UNIVERSITY OF CALIFORNIA,
IRVINE

Development and Application of a Spin-symmetry Breaking Algorithm for *Ab Initio* Non-adiabatic Molecular Dynamics Simulations

DISSERTATION

submitted in partial satisfaction of the requirements
for the degree of

DOCTOR OF PHILOSOPHY

in Chemistry

by

Jordan C. Vincent

Dissertation Committee:
Professor Filipp Furche, Chair
Professor Craig Martens
Professor Sergey Nizkorodov

2016

DEDICATION

To my best friend and life partner, Adriana.

TABLE OF CONTENTS

LIST OF FIGURES

LIST OF TABLES

ACKNOWLEDGMENTS

First and foremost I thank my thesis advisor, Professor Filipp Furche. Your excellence as a scientist may only be superceded by your strength as a human being. Without a doubt, your unwavering support throughout my unusual journey as a graduate student made this work possible. For as far back as I can remember I had a yearning to understand nature on a fundamental level. Theoretical chemical research is undeniably the best route toward that understanding. The privilege I have had to conduct my thesis work in this field is in many ways thanks to you. While working with you, I have grown immensely not only as a scientist but as a person. At times my path was riddled with self-doubt, however your belief in me helped drive me through to the end. Thank you.

Thank you to my dissertation committee Professor Sergey Nizkorodov and Professor Craig Martens. Your support and enduring patience have been invaluable to me. My ability to finish this work would not be possible without your input and encouragement. Thank you to Professor Vladimir Mandelshtam for your support when I was a new graduate student many years ago, and now for your willingness to step in as committee member at the last minute.

To my former advisor, Professor Doug Tobias. Your support and guidance throughout the years has been invaluable. I have learned so much doing research with you, and you have helped keep my passion for molecular dynamics alive. Thank you.

The Furche research group has been a supportive scientific family. A special thanks to Enrico Tapavicza. Your guidance and mentorship since day one in the Furche group has been crucial for my development as a computational chemist. You introduced me to the world of non-adiabatic dynamics, and it was your work upon which I have built my methodology. I thank Mikko Muuronen for useful discussions, encouragement, and support in writing this thesis. To the Furche post-docs, Shane Parker, Vamsee Voora, and Greg Bellchambers. Thank you for the helpful discussions, edits, and support within and outside of the office. To my fellow graduate students Jeb Bates, Brandon Krull, Matt Agee, Guo Chen, Saswata Roy, Sree Ganesh, and Luke Mohanam, you are an awesome group of guys whom I am proud to call colleagues. In particular, thank you to Saswata for the insightful conversations. Guo, your broad knowledge in theoretical methods and computer software have been an invaluable resource for me. Matt, you are undoubtedly the person I have spent the most time with in the past two years, besides my wife. You have been an incredible office mate and an excellent person. Thank you for putting up with me. Brandon, your support throughout the years has been incredible. Thank you for all the helpful encouragement, discussions, and feedback. To Alex Le, Jason Yu, Alan Chan, and Brian Nguyen, thank you for making this group even more solid. Finally, thanks to my students Kirk Pearce and Zayyan Takkieddine. Teaching has been a fulfilling endeaver which has repeatedly served as a powerful tool for my own learning.

To my parents Dale and Diane, thank you for your encouragement and support throughout the years. To my brothers and sisters who constantly encourage me to pursue my goals,

no matter how seemingly difficult they might be. I thank my family-in-law, Margoth, Luis Sr. and Luis Jr. Echeverria, who have been a home away from home.

I thank my friends, especially Adam Van Wart and Rose Philipps, who have been there through the best and worst times. You have always been there to pick me up when I was down, and to celebrate when I was up. Our discussions on science and life have been constant encouragement to me.

Finally, I thank the financial support of the National Science Foundation through grant award CHE-0909227 and the Deparment of Energy under Award DE-SC0008694, without which my endeavor to do science while feeding myself might have been impossible.

Section 3.3 contains excerpts reprinted with permission from Michael J. G. Peach, Matthew J. Williamson, David J. Tozer, Influence of Triplet Instabilities in TDDFT. *Journal of Chemical Theory and Computation*. Copyright 2011 American Chemical Society. Chapters 1, 3 and 4 contain excerpts from Jordan C. Vincent, Mikko Muuronen, Kirk C. Pearce, Luke N. Mohanam, Enrico Tapavicza, Filipp Furche, That Little Extra Kick: Non-adiabatic Effects in Acetaldehyde Photodissociation. Reproduced in part with permission from *Journal of Physical Chemistry Letters*, submitted for publication. Unpublished work copyright 2016 American Chemical Society.

CURRICULUM VITAE

Jordan C. Vincent

EDUCATION

Doctor of Philosophy in Chemistry **2016**
University of California, Irvine *Irvine, California*

Master's of Science in Chemistry **2011**
University of California, Irvine *Irvine, California*

Bachelor of Science in Chemistry **2007**
Saint Cloud State University *Saint Cloud, Minnesota*

Bachelor of Arts in Mathematics **2007**
Saint Cloud State University *Saint Cloud, Minnesota*

RESEARCH EXPERIENCE

Graduate Research Assistant **2013–2016**
University of California, Irvine *Irvine, California*

Junior Specialist **2012**
University of California, Irvine *Irvine, California*

Graduate Research Assistant **2007–2011**
University of California, Irvine *Irvine, California*

SELECTED TEACHING EXPERIENCE

Teaching Assistant
General Chemistry Lab (CHEM 1LC)
University of California, Irvine **2016**

Mentor
Computational Chemistry Research
University of California, Irvine **2014–2016**

Teaching Assistant
Classical Mechanics (CHEM 230)
University of California, Irvine **2013**

Tutor
Chemistry, Physics, and Calculus
Charles R. Drew University, Los Angeles **2012**

Teaching Assistant
Scientific Computing Skills (CHEM 5)
University of California, Irvine **2010**

REFEREED JOURNAL PUBLICATIONS

1) *Specific ion interactions with aromatic rings in aqueous solutions: Comparison of molecular dynamics simulations with a thermodynamic solute partitioning model and Raman hydration shell spectroscopy*. J.C. Vincent, S. Matt, B. Rankin, R. D'Auria, J.A. Freites, D. Ben-Amotz, D.J. Tobias, *Chem. Phys. Lett.*, **2015**, *638*, pp 1-8

2) *Ab initio non-adiabatic molecular dynamics*. E. Tapavicza, G.D. Bellchambers, J.C. Vincent, F. Furche, *Phys. Chem. Chem. Phys.*, **2013**, *15*, pp 18336-18348

3) *Ion specificity at the peptide bond: Molecular dynamics simulations of N-methylacetamide in aqueous salt solutions*. J. Heyda, J.C. Vincent, D.J. Tobias, J. Dzubiella, P. Jungwirth, *J. Phys. Chem. B*, **2010**, *114 (2)*, pp 1213-1220

REFEREED JOURNAL PUBLICATIONS SUBMITTED OR UNDER REVIEW

1) *That Little Extra Kick: Non-adiabatic Effects in Acetaldehyde Photodissociation*. J.C. Vincent, M. Muuronen, K.C. Pearce, L.N. Mohanam, E. Tapavicza, F. Furche, *J. Phys. Chem. Lett.*, **2016**

REFEREED CONFERENCE PUBLICATIONS

Non-adiabatic molecular dynamics with spin-symmetry breaking for describing photochemistry of acetaldehyde **November 2015**
45th ACS Western Regional Meeting

ACADEMIC SERVICE AND CONTRIBUTIONS

Student representative School of Physical Sciences **2008–2011**
Associated Graduate Students, University of California *Irvine, California*

Student representative to the Student Regent Selection Committee **2010–2011**
University of California Student Association

Student representative to the Legislative Committee **2010–2011**
University of California Student Association

ABSTRACT OF THE DISSERTATION

Development and Application of a Spin-symmetry Breaking Algorithm for *Ab Initio* Non-adiabatic Molecular Dynamics Simulations

By

Jordan C. Vincent

Doctor of Philosophy in Chemistry

University of California, Irvine, 2016

Professor Filipp Furche, Chair

Fast photochemical processes are central to a number of problems challenging chemists today. Such problems include atmospheric air pollution driven by solar radiation[2], development of photocatalysts for clean energy sources[3] and photodynamic therapies for treatment of diseases such as cancer[1], and light-driven biological phenomena such as vision[1] and vitamin D photosynthesis[4]. Continued improvement of computational methods which can describe and predict such photochemical processes is thus essential. Accordingly, this thesis focuses on two main topics: 1) The development of a spin-symmetry breaking algorithm which for the first time enables homolytic bond cleavage in 'on the fly' density functional non-adiabatic molecular dynamics simulations, and 2) a benchmarking application of the spin-symmetry breaking algorithm to acetaldehyde photochemistry.

Following a brief overview of the challenges inherent within this work, chapter 2 introduces fast photochemical processes and the theoretical foundations of *ab inito* non-adiabatic molecular dynamics methods. In Chapter 3, a new algorithm for breaking spin-symmetry within linear response time-dependent density functional theory is derived and implemented in the quantum-chemical software suite Turbomole[5]. H_2 is used to illustrate the key features of the algorithm, which are: 1) Stability analysis is used to identify critical

points on the PES, 2) tight convergence thresholds are used only near triplet instabilities, and 3) adaptive time stepping in the vicinity of triplet instabilities is employed to conserve total energy.

An application of the spin-symmetry breaking algorithm to acetaldehyde photochemistry is then discussed in Chapter 4. Ensembles of approximately 400 trajectories in the ground state and 400 trajectories initialized in the excited state are simulated. Compared to experiment, the spin-symmetry breaking algorithm yields qualitative accuracy for computed branching ratios and total kinetic energy probability distributions. Additionally, two dissociation mechanisms are identified and discussed: The non-transition state theory, "roaming", mechanism and new triple-fragmentation mechanisms. Finally, the spin-symmetry breaking algorithm reveals that an improved description of acetaldehyde photodissociation mechanisms may require inclusion of excited state dynamics.

BO-SBA	Spin-symmetry breaking algorithm for direct ground state dynamics
CCSD	Coupled-cluster singles and doubles
CF	Coulson-Fischer point
COM	Center of mass
DFT	Density Functional Theory
FSSH	Tully's fewest switches surface hopping algorithm
IC	Internal conversion
KS	Kohn-Sham Density Functional Theory
LR-TDDFT-SH	Linear response time-dependent density functional theory with surface hopping
MO	Molecular orbital
NACV	Non-adiabatic coupling vector
NMD	Non-adiabatic molecular dynamics
PBE	Exchange-correlation functional of Perdew, Burke, and Ernzerhof
PBE0	PBE with 25% exact exchange
PES	Potential energy surface
RHF	Restricted Hartree-Fock
RKS	Restricted Kohn-Sham
SCF	Self-consistent field
SE	Schrödinger equation
SH-SBA	Spin-symmetry breaking algorithm with Tully's fewest switches surface hopping
TDA	Tamm-Dancoff Approximation
TKER	Total kinetic energy release of momentum-matched pairs
TST	Transition state theory
TS	Transition state
UHF	Unrestricted Hartree-Fock
UKS	Unrestricted Kohn-Sham
ZPE	Zero-point energy

Table 1: Abbreviations used heavily throughout this thesis

Chapter 1

Overview

Homolytic bond breaking is important in photochemistry, however single-reference methods are known to produce high energies for dissociation fragments[6] oftentimes leading to bound states in *ab initio* molecular dynamics simulations. For this reason multi-reference methods such as the complete active space self-consistent field (CASSCF) method and multi-reference configuration interaction have been employed to describe such bond breaking[7–9]. However, these methods scale exponentially with system size and thus make it difficult to simulate full dimensional 'on the fly' dynamics on systems larger than 10 atoms. A more practical approach is to use single-reference density functional methods with spin-symmetry breaking. This approach has been utilized in the ground state in recent simulations of electron impact mass spectrometry on organic polyradicals with much success[10]. In this thesis a method is developed which takes advantage of the good scaling and description of homolytic bond cleavage in spin-symmetry broken single-reference methods. For the first time, I demonstrate that ground state spin-symmetry breaking may be augmented with efficient time-dependent density functional theory to describe excited state and non-adiabatic processes to produce homolytic bond cleavage in an application to acetaldehyde photochemistry.

Chapter 2

Background

Portions of Section 2.4 follow arguments and notation from Domke, Yarkony, and Koppel, ed.[11]. In Section 2.5 the Hartree-Fock Method is summarized akin to the derivation by Szabo and Ostlund[12] and Density Functional Theory is summarized in the spirit of Koch and Holthausen[13]. Sections 2.5.3, 2.6, and 2.6.3 follow portions of Tapavicza, Bellchambers, Vincent, and Furche[14]. Additionally, the latter section follows arguments by Tully[15].

2.1 Introduction

In this chapter fast photodissociation dynamics is defined and introduced. Then, theoretical background for a spin-symmetry breaking algorithm (SBA) is introduced and fundamental relations are defined and formulated. In Section 2.4 the Born-Oppenheimer BO approximation is formulated. Atomic units are used throughout. Next, two general methods for computing the PES are presented in Section 2.5: 1) Wave function based methods in Section 2.5.1, and 2) density functional methods in Section 2.5.3. Then, efficient linear response time-dependent density functional theory (LR-TDDFT) methods for computing excited states, gradients, and derivative couplings are presented in Section 2.5.3. Direct non-adiabatic molecular dynamics is then presented in Section 2.6. Tully's FSSH (Section 2.6.3) is then introduced as means for incorporating non-adiabatic effects in direct BO dynamics in large molecular systems. Finally, in Section 2.5.4 the Coulson-Fischer (CF) point[16] is identified as a crucial location on the potential energy surface (PES), beyond which open-shell and radical intermediates and products are formed in single reference wavefunction and density functional methods. In the event of homolytic bond cleavage, the PES in the vicinity of the CF point is sensitive to movement of the molecular phase point. Thus, a proper understanding of the PES in the neighborhood of the CF point is needed for a robust SBA; this constitutes the crux of the problems addressed in this thesis and is further discussed in Chapter 3.

2.2 Fast Photodissociation Dynamics

All photochemical processes ultimately begin with the absorption of light, which causes virtually instantaneous ($< 10^{-15}$ s) excitation of molecular systems from low energy rovibrational states into higher rovibrational states, as depicted in Fig. (2.1). After light

Process	Time scale (s)
Absorption	$< 10^{-15}$
IC	$10^{-15} - 10^{-9}$
Bond cleavage	10^{-11}
Fluorescence	$10^{-12} - 10^{-6}$
Spin-orbit coupling/ISC	10^{-10}
Phosphorescence	$10^{-6} - 10$

Table 2.1: Light-induced processes, and their time scales[1].

absorption, a number of different processes may occur. Table (2.1) shows the time scale of major photoprocesses in molecules. "Fast" processes compete on the 10^{-12} s time scale and include internal conversion (IC), fluorescence, and dissociation. "Slow" processes, which compete on the 10^{-6} s time scale, include inter-system crossing (ISC), emission of light (phosphorescence), or further internal conversion and dissociation. Slow processes are beyond the scope of this work.

For many systems, excitations beyond the first excited state, S_n (n>1), will result in fast internal conversion to the first excited state, S_1. This fast IC is attributed to Kasha who stated "... the emitting level of a given multiplicity is the lowest excited level of that multiplicity"[19]; this is known as "Kasha's rule." Internal conversion processes usually take place on a timescale 10^4 times faster than spontaneous S_n (n>1) emission. Thus, most photodissociation, ISC, and fluorescence occur from the first excited state and essentially all photochemical activity occurs between the first singlet and triplet excited states and the ground state.

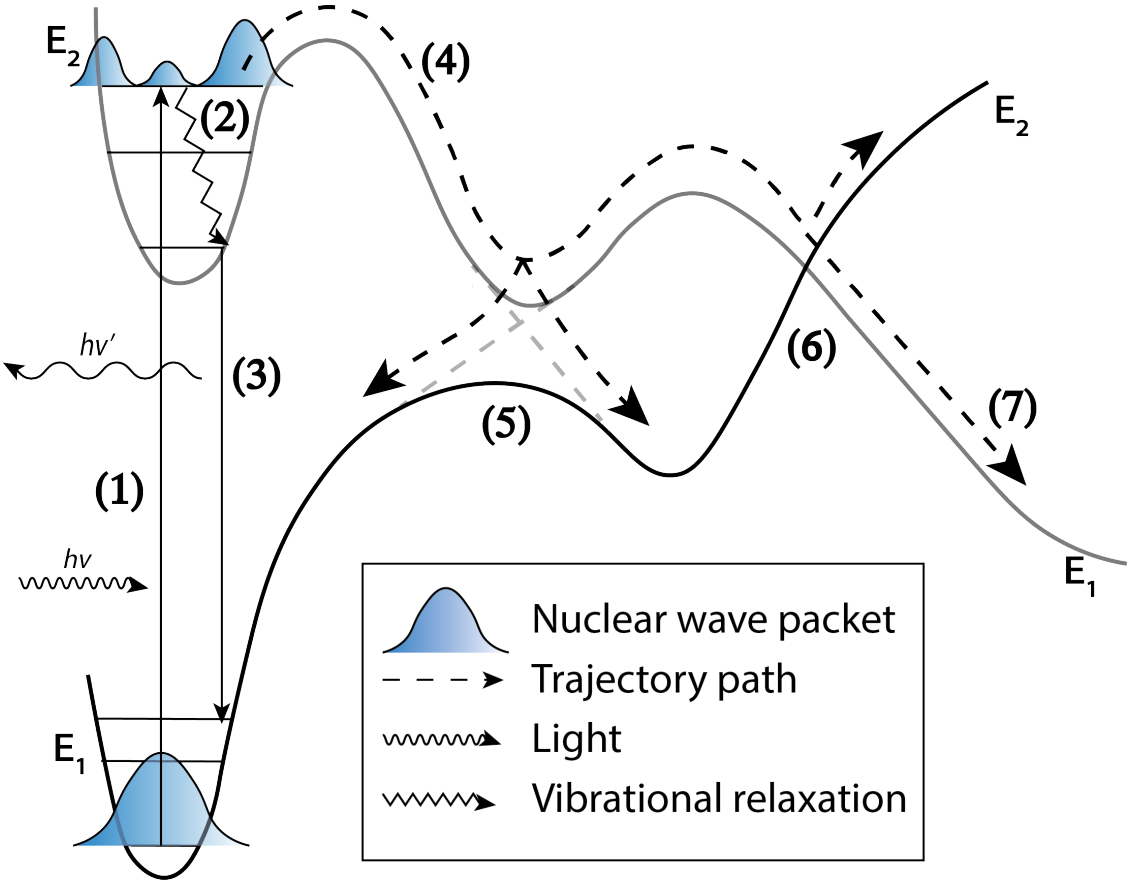

Figure 2.1: Schematic of some fast photochemical processes considered in this thesis. **(1)** Upon absorption of radiation with energy $h\nu$ at the Franck-Condon point[17,18] a molecule is excited from the ground vibrational and electronic state E_1 into an excited vibrational state of electronic state E_2. **(2)** Vibrational relaxition to the ground level of E_2 state is followed by, **(3)**, fluorescence. Fluorescence releases light with energy $h\nu'$, and the molecule is de-excited to the ground electronic state. **(4)** If fluorescence does not occur then the nuclear wave packet evolves in the excited state and passes by, **(5)**, an avoided crossing where the wave packet splits. The nuclear wave packet may encounter, **(6)**, a conical intersection where states E_2 and E_1 cross. **(7)** After internal conversion to the ground electronic state the trajectory evolves along a dissocative mode. Near avoided crossings, **(5)**, and conical intersections, **(6)**, the Born-Oppenheimer approximation breaks down due to strong coupling between E_1 and E_2.

The fast photochemical processes considered in this thesis may be summarized as follows:

$$\mathrm{ABC} + h\nu \rightarrow \mathrm{ABC}^* \rightarrow \mathrm{AB} + \mathrm{C} \tag{2.1}$$

$$\rightarrow \mathrm{ABC}^{*\prime} + h\nu'. \tag{2.2}$$

ABC is a molecular system which upon absorption of light, with frequency ν, becomes internally excited to ABC^* followed by either dissociation to products AB and C, or to internally excited $\mathrm{ABC}^{*\prime}$ along with emitted light of frequency ν'. The primed variables indicate a different internal energy from the intermediate and different emission frequency from the excitation in Eq. (2.1), respectively. Eq. (2.1) is directly computed and characterized with the methods developed and applied in this thesis. Process 2.2, while not characterized here, may be described using dynamical calculations employed herein. Eq. (2.1) is general and could represent, for example, the dissociation of gas phase species important in atmospheric processes, or may be the initialization step in a polymerization reaction. This type of chemistry may be understood theoretically, starting with the molecular Schrödinger equation, introduced in the following section.

2.3 Electronic Structure Methods

The time-dependent Schrödinger equation (SE)[20] for electrons and nuclei,

$$i\frac{\partial}{\partial t}\Psi(\boldsymbol{R},\boldsymbol{r},t) = H\Psi(\boldsymbol{R},\boldsymbol{r},t), \tag{2.3}$$

governs all molecular photodissociation dynamics. In Eq. (2.3), H is the molecular Hamiltonian, $\boldsymbol{R} = \{\boldsymbol{R}_1, \boldsymbol{R}_2, .., \boldsymbol{R}_K\}$ and $\boldsymbol{r} = \{\boldsymbol{r}_1, \boldsymbol{r}_2, .., \boldsymbol{r}_N\}$ are the nuclear and electronic

coordinates, respectively. $\boldsymbol{R}_\alpha$ is the three-dimensional coordinate vector for nucleus α, where the index α runs over all K nuclei. $\boldsymbol{r}_j$ is the coordinate vector for electron j, where the index j runs over all N electrons. Exact solution to Eq. (2.3) is impossible for molecules with more than a few atoms and thus approximations are necessary. The Born-Oppenheimer (BO) approximation[21] separates the electronic and nuclear motions, enabling solution to the electronic and nuclear problems.

A consequence of the BO approximation is the molecular potential energy surface (PES), which is a fundamental notion in chemical reactivity theory[22,23]. One of the most popular tools for describing chemical reactivity is transition state theory (TST)[24]. The central entity in TST is the activated complex transition state (TS), which is the molecular configuration connecting reactants and products through a minimum energy pathway. Armed with knowledge of the activated complex potential energy, local reactant and product minima, etc. on the PES[25,26], TST provides reaction rates and branching ratios, making it a powerful descriptive and predictive tool[26]. Yet there are several problems which require treatments beyond TST[25].: 1) The complexity of the PES grows exponentially with system size, making it difficult or impossible to identify reaction mechanisms in large molecular systems *a priori*[14], 2) nuclear motion drives (a) trajectory bifurcation for reaction pathways sharing the same TS[27] and b) coupling between potential energy surfaces which is a dominant process in photochemistry[23], and finally, 3) recently identified mechanisms, such as the "roaming" mechanism[25,28], do not have a well-defined TS.

The above stated problems have been addressed using a variety of approaches. For molecules with many degrees of freedom, 'on the fly' or direct dynamics methods enables step-by-step integration of the electronic and nuclear degrees of freedom along a trajectory. In this way, sampling of the PES can be done in an unbiased way, bifurcation events are addressed by including nuclear motion[29], and trajectories evolving through non-TS mechanisms are readily identified[30]. In the following sections theoretical foundations of

ab initio molecular dynamics methods are overviewed.

2.4 The Born-Oppenheimer Approximation

Eq. (2.3) trivially separates into time-dependent and time-independent parts. Solving the time-independent molecular Schrödinger equation,

$$H\Phi(\boldsymbol{R},\boldsymbol{r}) = E\Phi(\boldsymbol{R},\boldsymbol{r}), \tag{2.4}$$

constitutes the major theoretical challenge to describing molecular photochemistry. In Eq. (2.4) $\Phi(\boldsymbol{R},\boldsymbol{r})$ is the time-independent molecular wavefunction, and E is the energy. The non-relativistic Hamiltonian,

$$\begin{aligned} H = & -\frac{1}{2}\sum_{\alpha}\frac{\nabla_{\alpha}^{2}}{M_{\alpha}} \\ & + \left(\frac{1}{2}\sum_{\alpha\neq\beta}\frac{Z_{\alpha}Z_{\beta}}{|\boldsymbol{R}_{\alpha}-\boldsymbol{R}_{\beta}|} + -\frac{1}{2}\sum_{i}\nabla_{i}^{2} - \frac{1}{2}\sum_{\alpha j}\frac{Z_{\alpha}}{|\boldsymbol{R}_{\alpha}-\boldsymbol{r}_{j}|} + \frac{1}{2}\sum_{i\neq j}\frac{1}{|\boldsymbol{r}_{i}-\boldsymbol{r}_{j}|} + V_{ext}\right), \end{aligned} \tag{2.5}$$

fully describes fast photodynamic processes. The $\{\alpha,\beta\}$ run over all K nuclei and $\{i,j\}$ run over all N electrons. The first term in Eq. (2.5) is the nuclear kinetic energy where the αth nucleus has mass, M_{α}. The terms enclosed within parentheses collectively define the electronic Hamiltonian, H_{el},

$$H_{el} \equiv -\frac{1}{2}\sum_{i}\nabla_{i}^{2} - \frac{1}{2}\sum_{\alpha j}\frac{Z_{\alpha}}{|\boldsymbol{R}_{\alpha}-\boldsymbol{r}_{j}|} + \frac{1}{2}\sum_{ij}\frac{1}{|\boldsymbol{r}_{i}-\boldsymbol{r}_{j}|} + \frac{1}{2}\sum_{\alpha\neq\beta}\frac{Z_{\alpha}Z_{\beta}}{|\boldsymbol{R}_{\alpha}-\boldsymbol{R}_{\beta}|} + V_{ext}(t). \tag{2.6}$$

In Eq. (2.6) the first term is the total electronic kinetic energy, the second term is the attractive electron-nucleus Coulomb potential between the jth electron and the αth nucleus,

the third term is the electron-electron repulsion, the fourth term is the nuclear-nuclear Coulomb repulsion between nuclei α and β with charges Z_α and Z_β, respectively and $V_{ext}(t)$ is the time-dependent external potential. In the systems considered for this thesis, the external potential is set to zero.

2.4.1 Separating Electronic and Nuclear Motions

$$\Phi(\boldsymbol{R}, \boldsymbol{r}) = \sum_{i=1}^{\infty} \phi_i(\boldsymbol{r}; \boldsymbol{R}) \zeta_i(\boldsymbol{R}) \tag{2.7}$$

is an exact expansion of the molecular wavefunction, where the $\phi_i(\boldsymbol{r}; \boldsymbol{R})$ depend parametrically on the nuclear coordinates and satisfy the electronic Schrödinger equation,

$$H_{el}\phi_j(\boldsymbol{r}; \boldsymbol{R}) = E_j^{el}\phi_j(\boldsymbol{r}; \boldsymbol{R}). \tag{2.8}$$

E_j^{el} defines the potential energy surface, and the spin-functions are assumed to be absorbed into the electronic and nuclear parts of Eq. (2.7). Insertion of Eq. (2.7) into Eq. (2.4) and left multiplication of $\phi_j(\boldsymbol{r}; \boldsymbol{R})$ followed by integration over all electronic coordinates yields the coupled eigenvalue equation for nuclei,

$$[T_n + E_j^{el}(\boldsymbol{R})]\zeta_j(\boldsymbol{R}) - \sum_i \Lambda_{ji}\zeta_i(\boldsymbol{R}) = E\zeta_j(\boldsymbol{R}). \tag{2.9}$$

T_n is the nuclear kinetic energy operator given in Eq. (2.5). The coupling term in Eq. (2.9), Λ_{ji}, is given by

$$\Lambda_{ji} = \sum_{A=1}^{N} \frac{1}{2M_A}[2\vec{F}_{ji}^A \cdot \nabla_A + G_{ji}^A] \tag{2.10}$$

where

$$\vec{F}_{ji}^{A}(\boldsymbol{R}) = \langle \phi_j | \nabla_A \phi_i \rangle \tag{2.11}$$

is the first-order derivative coupling between BO states j and i along nuclear coordinate A, and

$$G_{ji}^{A}(\boldsymbol{R}) = \langle \phi_j | \nabla_A^2 | \phi_i \rangle \tag{2.12}$$

is the second-order derivative coupling. Setting $\Lambda_{ji} = 0$ for all $\{i, j\}$ gives rise to the BO adiabatic approximation which effectively separates the nuclear and electronic degrees of freedom[11,31]. The BO approximation is thus equivalent to viewing the electronic motion instantaneously responding to changes in the nuclear coordinates. Thus the intractable time-independent molecular Schrödinger equation (Eq. (2.4)) reduces to two tractable Schrödinger equations for the electrons (Eq. (2.8)) and nuclei,

$$[T_n + E_j^{el}(\boldsymbol{R})]\zeta_j(\boldsymbol{R}) = E\zeta_j(\boldsymbol{R}). \tag{2.13}$$

Hence, molecular dynamics may be viewed as a nuclear wave packet, ζ, evolving in the potential of electrons and nuclear-nuclear repulsion,E_j. This construction is illustrated in Fig. (2.1), where the nuclear wave packet evolves on multiple electronic PESs. For quantum nuclei solution of Eq. (2.13) yields the rotational, vibrational, etc. states of the nuclear wavefunction.

2.5 Calculating the Potential Energy Surface

Calculating the PES for the ground and excited states remains the computational bottleneck for *ab initio* methods. Two broad categories of *ab initio* methods exist: 1) Wavefunction

based methods and, 2) density functional methods. The Hartree-Fock (HF) approximation is foundational to almost all molecular wavefunction methods and provides many of the concepts used in both wavefunction and density functional methods. HF is introduced in Section 2.5.1. Kohn-Sham Density Functional Theory (KS-DFT) is the most widely used density functional method and provides the starting point for computing ground and excited states in an efficient manner; KS-DFT is introduced in Section 2.5.3.

2.5.1 Hartree-Fock Method

In the Hartree-Fock (HF) method the molecular wavefunction is approximated as a single Slater determinant composed of one electron spin-orbitals, $\chi(\boldsymbol{x})$.

$$\tilde{\phi}_0(\boldsymbol{x}_1, \boldsymbol{x}_2, .., \boldsymbol{x}_N) = (N!)^{-1/2} \begin{vmatrix} \chi_i(\boldsymbol{x}_1) & \chi_j(\boldsymbol{x}_1) & \cdots & \chi_k(\boldsymbol{x}_1) \\ \chi_i(\boldsymbol{x}_2) & \chi_j(\boldsymbol{x}_2) & \cdots & \chi_k(\boldsymbol{x}_2) \\ \vdots & \vdots & \ddots & \vdots \\ \chi_i(\boldsymbol{x}_N) & \chi_j(\boldsymbol{x}_N) & \cdots & \chi_k(\boldsymbol{x}_N) \end{vmatrix} \tag{2.14}$$

where each spin-orbital χ_i is a function of the spatial and spin-coordinates of the jth electron, $\boldsymbol{x}_j = \{\boldsymbol{r}_j, \omega_j\}$. $\boldsymbol{r}_j = \{r_j^x, r_j^y, r_j^z\}$ is in cartesian coordinates, and ω_j is the spin-coordinate. The N electrons occupy a subset of the K spin-orbitals, $\{\chi_i, \chi_j, .., \chi_k\}$, where K is the basis set size. Spin-orbitals are composed of a spatial part, $\psi(\boldsymbol{r})$, and a spin part, $\alpha(\omega)$ or $\beta(\omega)$:

$$\chi_i(\boldsymbol{x}) = \begin{cases} \psi_j(\boldsymbol{r})\alpha(\omega), \\ \text{or} \\ \psi_j(\boldsymbol{r})\beta(\omega). \end{cases} \tag{2.15}$$

When both α and β electrons are constrained to the same spatial function (molecular orbital), ψ_j, the resulting spin-orbitals are "restricted" and the subsequent treatment is restricted Hartree-Fock (RHF). The optimal molecular orbitals are determined via the Variational Principle,

$$\frac{\int d^K\boldsymbol{x}\tilde{\phi}_0^*(\boldsymbol{x})H^{el}\tilde{\phi}_0(\boldsymbol{x})}{\int d^K\boldsymbol{x}\tilde{\phi}_0^*(\boldsymbol{x})\tilde{\phi}_0(\boldsymbol{x})} \geq E_0. \tag{2.16}$$

The best approximation to the exact ground state of Eq. (2.4), $\phi_0(\boldsymbol{x})$, with exact ground state energy, E_0, minimizes the left-hand side of Eq. (2.16). $\tilde{\phi}_0(\boldsymbol{x})$ is the approximate molecular wavefunction, where the parametric dependence on the nuclear coordinates, $\boldsymbol{R}$, has been dropped.

The restricted treatment typically describes well closed-shell molecules near their equilibrium geometry [12]. But to describe closed-shell molecules away from their equilibrium geometry or open-shell systems in general, spatially unrestricted spin-orbitals must be

allowed,

$$\chi_i^{\alpha/\beta}(\boldsymbol{x}) = \begin{cases} \psi_j^{\alpha}(\boldsymbol{r})\alpha(\omega), \\ \text{or} \\ \psi_j^{\beta}(\boldsymbol{r})\beta(\omega). \end{cases} \tag{2.17}$$

$\psi_j^{\alpha}(\boldsymbol{r})$ is the spatial orbital for electron with α spin-function, and it is allowed to differ from the spatial orbital, $\psi_j^{\alpha}(\boldsymbol{r})$, corresponding to the β spin-function. Relaxing the constraint on the spatial orbitals leads to the unrestricted Hartree-Fock (UHF) method. An example of the results of RHF and UHF are given in application to H_2 bond dissocation, shown in Fig. (2.2). It is clear that away from the equilibrium bond distance, UHF describes H_2 better than RHF.

Near the equilibrium geometry of closed-shell molecules, the RHF and UHF methods will converge to the same solution. However, as the molecule moves away from its equilibrium geometry, as is the case in stretching the H_2 bond, the UHF solution will diverge from the RHF one. The locus of divergence is known as the Coulson-Fischer point[16], and it is there where the spin-symmetry "breaks."

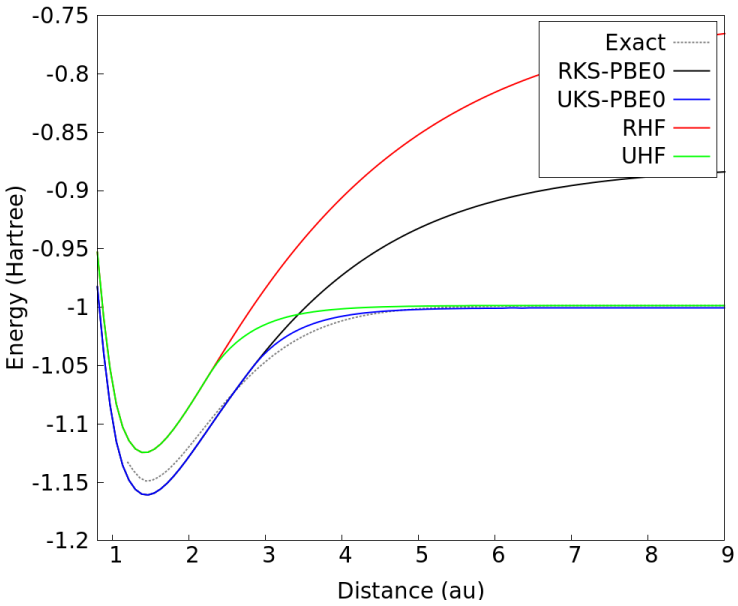

Figure 2.2: H_2 dissociation using RHF (red), UHF (green), RKS (black), UKS (blue), and exact CCSD (dotted) solutions. The Coulson-Fischer point is the bond length at which the UHF diverges from the RHF, and the UKS diverges from the RKS solutions. All calculations are performed in Turbomole[5] with def2-SV(P)[32] basis and DFT calculations use the PBE0[33] exchange-correlation functional.

2.5.2 Correlation Energy

The difference in energy between the UHF/RHF solutions and the exact solution, illustrated in Fig. (2.2), is the correlation energy,

$$E_0^{corr} = \tilde{E}_0 - E_0, \tag{2.18}$$

where $\tilde{E}_0$ is the ground state energy for the Hartree-Fock solution in the basis set limit, and E_0 is the exact ground state energy. In general, methods which can capture the correlation energy are necessary to predict quantitative energies, bond dissocation curves, etc. In density functional methods, however, correlation is captured more readily even within a single determinant approximation to the ground state. Density functional methods are discussed in the following section.

2.5.3 Density Functional Methods

According to the Hohenberg-Kohn Theorem[34], the exact ground state energy,

$$E[\rho] = T_e[\rho] + E_{ee}[\rho] + E_{en}[\rho, \boldsymbol{R}], \tag{2.19}$$

is a functional of the electron density,

$$\rho = K \int ... \int |\Psi(\boldsymbol{x}_1, ..., \boldsymbol{x}_K)|^2 d\boldsymbol{x}_1 ... d\boldsymbol{x}_K. \tag{2.20}$$

In Eq. (2.19) T_e is the kinetic energy functional, E_{ee} contains all two-electron contributions, and E_{en} contains the electron-nucleus terms. All coordinates but $\boldsymbol{r}_1$ are integrated out in Eq. (2.20). This is the foundation for density functional (DF) methods discussed below.

Ground State Properties from Kohn-Sham DFT

Kohn and Sham[35] sought to solve the many-body problem by mapping the interacting system onto a fictitious non-interacting system. This mapping is done by solving Kohn-Sham (KS) equations,

$$\left(-\frac{1}{2}\nabla^2 + V_{eff} \right) \phi_i = \epsilon_i \phi_i, \tag{2.21}$$

for the KS orbitals, ϕ_i. V_{eff} is the non-interacting potential and it follows directly from the KS construction and the Hohenberg-Kohn Theorem[34],

$$V_{eff}(\boldsymbol{r}_1) = \int \frac{\rho(\boldsymbol{r}_2)}{r_{12}} d\boldsymbol{r}_2 + V_{XC}(\boldsymbol{r}_1) - \sum_A^N \frac{Z_A}{r_{1A}}. \tag{2.22}$$

$V_{XC} = \delta E_{XC}/\delta\rho$ is the exchange-correlation potential which is the functional derivative of the exchange-correlation energy, E_{XC}. In the KS picture, the energy functional is written as

$$\begin{aligned} E[\rho] &= T_{KS}[\rho] + J[\rho] + E_{XC}[\rho] + E_{en}[\rho] \\ &= -\frac{1}{2}\sum_{i}^{K}\langle\phi_i|\nabla^2|\phi_i\rangle + \frac{1}{2}\int\int d\boldsymbol{r}_1 d\boldsymbol{r}_2 \frac{\rho(\boldsymbol{r}_1)\rho(\boldsymbol{r}_2)}{r_{12}} + E_{XC}[\rho] + \int d\boldsymbol{r} V_{en}\rho(\boldsymbol{r}). \end{aligned} \tag{2.23}$$

T_{KS} is the kinetic energy of the KS orbitals and J is the Hartree potential. E_{XC} and its potential V_{XC} have an unknown form, and are chosen within the Kohn-Sham picture so as to reproduce the exact ground state density of the real interacting system. E_{XC} contains all exchange, self-interaction, correlation, and residual kinetic energy not captured by T_{KS}.

Since the exact E_{XC} functional is unknown current approximate functionals are limited in their ability to properly describe bond dissociation[13,36]. An improved description of homolytic bond dissociation, in analogy to the Hartree-Fock method, occurs when the KS orbitals are allowed to be unrestricted (UKS). A comparison of the RKS and UKS solutions for H_2 bond dissocation are illustrated in Fig. (2.2). Similar to HF, RKS describes the ground state energy well near the equilibrium bond length, however as the bond stretches the UKS and RKS solutions diverge with UKS yielding a better description for homolytic bond cleavage beyond the Coulson-Fischer point. Both UKS and RKS do better than the respective UHF and RHF, this is largely due to the inclusion of electron correlation through the E_{XC} functional.

Excited State Properties From Time-Dependent Density Functional Theory

The excited state PESs are computed from the excitation frequencies, Ω_i, found by solving the time-dependent Kohn-Sham eigenvalue problem[37–40]:

$$\left[\begin{pmatrix} \boldsymbol{A} & \boldsymbol{B} \\ \boldsymbol{B} & \boldsymbol{A} \end{pmatrix} - \Omega_n \begin{pmatrix} \mathbf{1} & \mathbf{0} \\ \mathbf{0} & -\mathbf{1} \end{pmatrix}\right] \begin{pmatrix} \boldsymbol{X}_n \\ \boldsymbol{Y}_n \end{pmatrix} = \mathbf{0}, \tag{2.24}$$

where $\boldsymbol{X}_n$ and $\boldsymbol{Y}_n$ are the transition density vectors, Ω_n is the ground $\rightarrow$ nth state excitation, and matrices $\boldsymbol{A}$ and $\boldsymbol{B}$ are the orbital rotation Hessians are[14],

$$(\boldsymbol{A}+\boldsymbol{B})_{ia\sigma,jb\tau} = \delta_{\sigma\tau}\delta_{ij}\delta_{ab}(\epsilon_{a\sigma} - \epsilon_{i\sigma}) \tag{2.25}$$

$$+ 2(ia\sigma|jb\tau) + 2f^{XC}_{ia\sigma jb\tau} - c_x\delta_{\sigma\tau}[(ja\sigma|ib\sigma) + (ab\sigma|ij\sigma)], \tag{2.26}$$

and

$$(\boldsymbol{A}-\boldsymbol{B})_{ia\sigma,jb\tau} = \delta_{\sigma\tau}\delta_{ij}\delta_{ab}(\epsilon_{a\sigma} - \epsilon_{i\sigma}) + c_x\delta_{\sigma\tau}[(ja\sigma|ib\sigma) - (ab\sigma|ij\sigma)] \tag{2.27}$$

where $(ia\sigma|jb\tau)$ is the Mulliken notation for the two-electron repulsion integral, c_x is the hybrid mixing coefficient, and $f^{XC}_{ia\sigma jb\tau}$ is the matrix element of the exchange-correlation kernal. In the adiabatic approximation

$$f^{XC}_{ia\sigma jb\tau} = \int d^3r d^3r' \phi^*_{k\sigma}(\boldsymbol{r})\phi_{l\sigma}(\boldsymbol{r}) \left(\frac{\delta^2 E_{XC}}{\delta\rho_\sigma(\boldsymbol{r})\delta\rho_\tau(\boldsymbol{r}')}\right) \phi^*_{n\tau}(\boldsymbol{r})\phi_{m\tau}(\boldsymbol{r}). \tag{2.28}$$

where the second order functional derivative is evaluated at the ground state density. $\phi_{k\sigma}(\boldsymbol{r})$ are the ground state KS orbitals, i, j and a, b represent the occupied and virtual orbitals, respectively. $\sigma = \alpha, \beta$ is the spin variable, and k, l, m and n indicate general orbitals. Due to algorithms which scale with system size N as $\mathcal{O}(N^2)$, TDDFT response theory methods are efficient and relatively accurate and are thus the methods of choice for computing

excitation energies, non-adiabatic couplings, and gradients for direct dynamics[14,41].

2.5.4 Stability Analysis

The Coulson-Fischer point may be located by performing a stability analysis. There exists an unrestricted KS solution when the ground state energy of the RKS solution becomes unstable with respect to variation of the molecular orbitals,

$$\frac{d^2}{dx^2}E(x) = \frac{d^2}{dx^2}\langle\tilde{\phi}_0|U^\dagger(x)H_{el}U(x)|\tilde{\phi}_0\rangle < 0, \tag{2.29}$$

where x is a parameter corresponding to orbital rotations through the unitary transformation, $U(x)$, and its conjugate transpose, $U^\dagger(x)$. Eq. (2.29) is satisfied when the eigenvalues of the super matrix,

$$\begin{pmatrix} \boldsymbol{A} & \boldsymbol{B} \\ \boldsymbol{B} & \boldsymbol{A} \end{pmatrix}, \tag{2.30}$$

are all positive[38]. The $\boldsymbol{A}$ and $\boldsymbol{B}$ matrices were defined in the previous section. When the lowest eigenvalue of Eq. (2.30) is negative, an instability occurs. When negative, eigenvalues correspond to rotations of triplet excitation character, and there exists a *triplet instability*, else the eigennvalues corresponds to rotations of singlet excitation character and is called a *singlet instability*.

2.6 *Ab initio* Non-adiabatic Molecular Dynamics

2.6.1 Classical Nuclei

In *ab initio* direct molecular dynamics the electrons evolve according to the time-dependent electronic Schrödinger equation,

$$i\frac{\partial}{\partial t}\Phi(\boldsymbol{r},t;\boldsymbol{R}) = H_{el}\Phi(\boldsymbol{r},t;\boldsymbol{R}), \tag{2.31}$$

and Eq. (2.31) is solved at each nuclear configuration, $\boldsymbol{R}$. The nuclei are treated classically according to Newton's equations of motion,

$$\begin{aligned} F_i &= -\frac{dE_j^{el}(\boldsymbol{R})}{dR_i} \\ &= M_\alpha \ddot{R}_i \end{aligned} \tag{2.32}$$

where M_α is the mass, R_i is the coordinate along the ith degree of freedom, and $\ddot{R}_i$ is the second order time derivative of the ith nuclear coordinate. *Ab initio* molecular dynamics integrated on a single PES is valid when it is well separated in energy from other PESs. However, in regions of strong coupling between two or more PESs, the BO approximation breaks down and non-adiabatic molecular dynamics (NMD) methods are required[14].

2.6.2 Breakdown of the Born-Oppenheimer Approximation

With the Hellmann-Feynman Theorem[42,43] and the conditions,

$$\langle\phi_j|\nabla\phi_i\rangle = \langle\phi_j\nabla|\phi_i\rangle, \tag{2.33}$$

and

$$\langle \phi_j | \phi_i \rangle = \delta_{ji}, \tag{2.34}$$

the first-order derivative couplings may be written as

$$F_{ji} = \langle \phi_j | \nabla \phi_i \rangle \tag{2.35}$$

$$= \frac{\langle \phi_j | \nabla H_{el} | \phi_i \rangle}{E_i - E_j}. \tag{2.36}$$

Eq. (2.35) implies the derivative couplings becomes large near avoided crossings and thus cannot be neglected in Eqs. (2.9) and (2.10). This constitutes a breakdown in the BO approximation and therefore derivative couplings must be considered near avoided crossings and conical intersection (see Fig. (2.1)). In photodissociation dynamics regions of strong coupling between PESs account for internal conversion.

One of the most widely used NMD methods for incorporating non-adiabicity is Tully's fewest switches surface hopping (FSSH). FSSH maintains the BO picture of the PES and incorpores non-adiabatic effects by including the first-order non-adiabatic derivative couplings[15].

2.6.3 Fewest Switches Surface Hopping

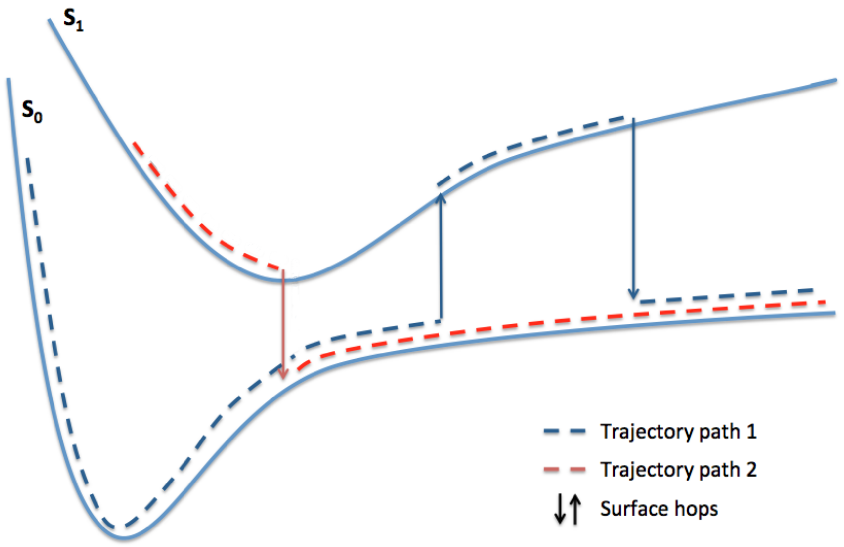

Figure 2.3: Schematic representation of Tully's fewest switches surface hopping algorithm. Wave packet dynamics are modelled by ensembles of mixed quantum-classical trajectories hopping between potential energy surfaces. The dashed lines represent two different trajectories: One begins in the ground state and encounters a region of strong coupling and subsequently hops back and forth between the excited and ground state. In a similar way another trajectory starts in the excited state in hops in region of strong coupling.

One of the most popular methods for incorporating non-adiabatic effects in *ab initio* molecular dynamics simulations is Tully's fewest switches surface hopping algorithm[14,15]. In this approach classical nuclei are propagated on single PESs and non-adiabatic effects are accounted for by stochastic hopping of the trajectory between PESs near regions of strong coupling (see Fig. (2.3)). To see this, first the time-dependent electronic wavefunction is expanded in a BO basis, $\phi_j(\boldsymbol{r};\boldsymbol{R})$,

$$\Psi(\boldsymbol{r},t;\boldsymbol{R}) = \sum_j c_j(t)\phi_j(\boldsymbol{r};\boldsymbol{R}) \tag{2.37}$$

and the time-dependent wavefunction is inserted into Eq. (2.31). This leads to the coupled differential equations for the state coefficient column vector, $\boldsymbol{c}$,

$$i\dot{\boldsymbol{c}} = (\boldsymbol{H} - i\boldsymbol{Q})\boldsymbol{c}. \tag{2.38}$$

The elements of $\boldsymbol{c}$ are the time dependent state coefficients $c_j(t)$ from Eq. (2.37). $\dot{\boldsymbol{c}}$ is the time-derivative of the state coeffecient vector, $\boldsymbol{H}$ is the electronic Hamiltonian matrix, and $\boldsymbol{Q}$ is defined as

$$\begin{aligned} Q_{mn} &= \langle \phi_m | \frac{\partial}{\partial t} \phi_n \rangle \\ &= \dot{\boldsymbol{R}} \cdot \boldsymbol{F}_{mn} \end{aligned} \tag{2.39}$$

where $\dot{\boldsymbol{R}}$ is the nuclear velocity and $\boldsymbol{F}_{mn}$ is the non-adiabatic derivative coupling between PESs m and n. The off-diagonal $c_i c_j^*$, $i \neq j$, are referred to as the coherences and while the diagonal elements are the state populations. The matrix elements of Eq. (2.38) are

$$i\frac{d}{dt} c_i c_j^* = \sum_l \left(c_i c_j^* [H_{il} - iQ_{il}] - c_i c_l^* [H_{lj} - iQ_{lj}] \right), \tag{2.40}$$

and the diagonal elements of Eq. (2.40) represent the change in state population. The diagonals may be expressed as

$$\frac{d}{dt} c_i c_i^* = \sum_{l \neq i} b_{il}, \tag{2.41}$$

where

$$b_{il} = 2\Im c_i c_l^* [H_{il} - iQ_{il}] - 2\Re [c_i c_l^* iQ_{il}]. \tag{2.42}$$

In a BO basis the off-diagonal element of $\boldsymbol{H}$ are zero, and Eq. (2.42) becomes a function of the derivative couplings and nuclear velocities only. Thus, changes in state population are

driven only through the derivative couplings. Tully[15] argued that the transition probability from state $i \rightarrow j$ for a two state system may be expressed in terms of the change in state populations, Eq. (2.41), as

$$g_{ij} = \frac{b_{ji}\Delta t}{c_i c_i^*}, \tag{2.43}$$

for sufficiently small time step Δt. When the probability g_{ij} is greater than a random number $\in [0, 1]$ then a trajectory "hops" from state $i \rightarrow j$ and dynamics continues on PES j. When a hop occurs, the nuclear momenta are scaled along the direction of the non-adiabatic coupling vector $\boldsymbol{F}_{mn}$ in order to conserve total energy[44–47]. In this way, the nuclear wavepacket is modelled as an ensemble of classical trajectories which stochastically hop between PESs. FSSH preserves several desirable attributes of *ab initio* molecular dynamics: 1) The electronic state populations, c_i, are accurately reproduced in an ensemble of trajectories, 2) trajectory splitting occurs in regions of strong coupling, 3) total energy conservation is satisfied, and 4) detailed balance is approximately satisfied[14]. More accurate methods such as Multiple Spawning[48] include quantum nuclei and require significantly more computational resources. The FSSH algorithm allows incorporating nonadiabaticity without loss of the Born-Oppenheimer picture and the PES. For photochemistry, this means that internal conversion and intersystem crossing occur via hopping between states.

Chapter 3

Spin-symmetry Breaking Algorithm

Portions of this chapter from J.C. Vincent, M. Muuronen, K.C. Pearce, L.N. Mohanam, E. Tapavicza, and F. Furche, That Little Extra Kick: Non-adiabatic Effects in Acetaldehyde Photodissociation. Reproduced in part with permission from *Journal of Physical Chemistry Letters*, submitted for publication. Unpublished work copyright 2016 American Chemical Society.

Section 3.3 contains excerpts reprinted with permission from Michael J. G. Peach, Matthew J. Williamson, David J. Tozer, Influence of Triplet Instabilities in TDDFT. *Journal of Chemical Theory and Computation*. Copyright 2011 American Chemical Society.

The material in this chapter is based upon work supported by the Department of Energy under Award DE-SC0008694 and the National Science Foundation under award CHE-0909227.

3.1 Introduction

In this chapter an algorithm is developed which enables for the first time homolytic bond cleavage within linear-response time-dependent density functional theory with Tully's[15] fewest switches surface hopping (LR-TDDFT-SH). Near critical points on the potential energy surface (PES) a number of obstacles are encountered with spin-restricted simulation methods. A spin-symmetry breaking algorithm (SBA) is developed to overcome these limitations. The key features of the SBA are: 1) Stability analysis for identifying critical points, also known as Coulson-Fischer (CF) points, on the PES; 2) adaptive time stepping near the CF point for energy conservation; 3) tightened convergence thresholds near the CF point for energy conservation, and 4) forced spin-symmetry breaking beyond the CF point.

The SBA has been developed specifically for LR-TDDFT-SH within the Tamm-Dancoff approximation (TDA) and has been implemented in Turbomole[5]. A recent implementation by Spörkel and Thiel[49] uses adaptive time-stepping for surface hopping simulations with multi-reference wave function methods. However, to the author's knowledge the SBA is the first to treat homolytic bond breaking in single-reference surface hopping direct dynamics. The implementation presented here is predicated upon the LR-TDDFT-SH implementation by Tapavicza *et al.*[4,50] which has described well spin-restricted photochemical processes.

The presentation in this chapter is as follows: H_2 is considered as a simple model to highlight key features of the method. The plausibility for using a spin-symmetry broken reference in surface hopping simulations is discussed. This is followed by an overview of the performance of DFT/TDDFT methods for describing H_2 bond cleavage. Then, obstacles which are overcome by the SBA are analyzed, starting with the characterization and identification of the CF point. Forced spin-symmetry breaking is then employed

beyond the CF point. Constant integration time steps for propagation of the nuclei are found to incur instabilities near the CF point. This is overcome by adaptive time stepping. Additionally, convergence thresholds are required near the CF point to ensure energy conservation. Finally, the SBA is summarized with a flowchart. Unless stated otherwise all calculations are performed using Turbomole[5]. The SBA is then benchmarked in Chapter 4.

3.2 H_2 model

3.2.1 Plausibility of Broken Spin-symmetry and Surface Hopping

Giesbertz and Baerends[51] point out that TDDFT fails to describe homolytic bond breaking in the first singlet excited state. However, as shown in the lower left panel of Fig. (3.1), this failure only arises for spin-restricted TDDFT, while the TDA[52] results are consistent with the exact results shown in Fig. (3.2). Li *et al.*[53] assert that excitation energies from spin-symmetry broken reference states are meaningless within LR-TDDFT. However, the upper left and lower right panels of Fig. (3.1) and the left panel of Fig. (3.2) suggest excited states from a spin-symmetry broken reference yield qualitative accuracy for the excited state PES. Furthermore, my results presented in the following chapter suggest that spin-symmetry broken ground and excited states perform reasonably well in surface hopping dynamics.

3.2.2 Performance of DFT Methods

Performance of two exchange-correlation functionals are compared in Fig. (3.1). The general gradient approximation PBE[54] functional and the PBE with 25% exact exchange, PBE0[33], are compared. Both restricted Kohn-Sham (RKS) and UKS, rPBE and uPBE,

respectively, and rPBE0/uPBE0 functionals are compared to each other in the upper and lower right panels of Fig. (3.1). Excitations are computed within the Tamm-Dancoff approximation (TDA)[41]. In the ground state, while rPBE performs slightly better in the asymptotic region, the difference between it and rPBE0 is small, with a maximum difference of approximately 0.02 Hartree at a bond length of 9 au. The difference in performance between the two is even less for the first singlet excitations from a restricted reference, with a maximum difference of approximately 0.01 Hartree at a bond length of 5 au. uPBE and uPBE0 are virtually indistiguishable in the lower right panel of Fig. (3.1). However, both uTDA/PBE and uTDA/PBE0 diverge from the rTDA calculation beyond the CF point, which is indicated by a vertical red line. u/rTDA and u/rTDDFT are compared in the upper and lower left panels of Fig. (3.1). rTDDFT/PBE0 fails in accord with Giesbertz and Baerend[51], however uTDDFT/PBE0 describes the first excited state with similar accuracy as the uTDA/PBE0 (upper left panel). Furthermore, the uTDDFT/PBE0 is relatively unnaffected at the CF point. However, due to known instabilites in TDDFT[41], the TDA is used throughout this thesis.

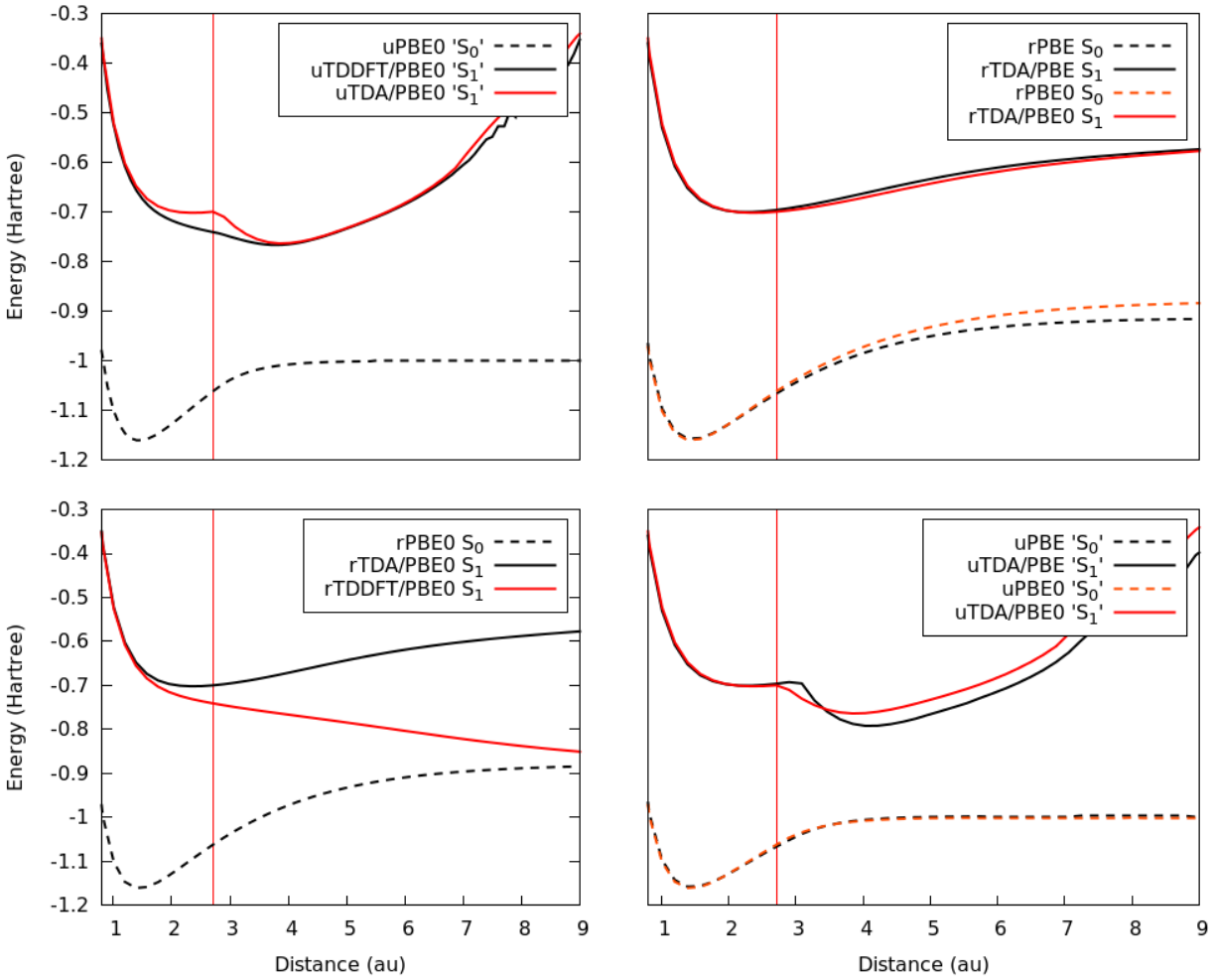

Figure 3.1: Comparisons of ground and excited state PESs for H_2 within TDA/TDDFT and PBE/PBE0. The vertical line indicates the CF point in the PBE0 ground state. **Upper left**: uTDDFT/PBE0 (solid black) and uTDA/PBE0 (solid red) are compared. The uPBE0 reference is the black dashed curve. **Lower left**: TDDFT (solid red) and TDA (solid black) with spin-restricted reference (dashed) are compared. **Upper right**: r/TDA/PBE0 (red solid/dashed) and r/TDA/PBE (black solid/dashed) are compared. **Lower right**: u/TDA/PBE0 (red solid/dashed) and u/TDA/PBE (black solid/dashed) are compared. All calculations are performed with a def2-SV(P) basis.

Fig. (3.2) shows that the rTDA/PBE0 describes the excited state well when compared to the exact result, however when compared to the CCSD excitatation it over binds by approximately 0.01 Hartree near the equilibrium geometry. uTDA/PBE0 performs very well for ground state energies, and similar to rTDA/PBE0 in the excited state near the equilibrium geometry, but diverges abruptly from the CCSD and rTDA/PBE0 beyond

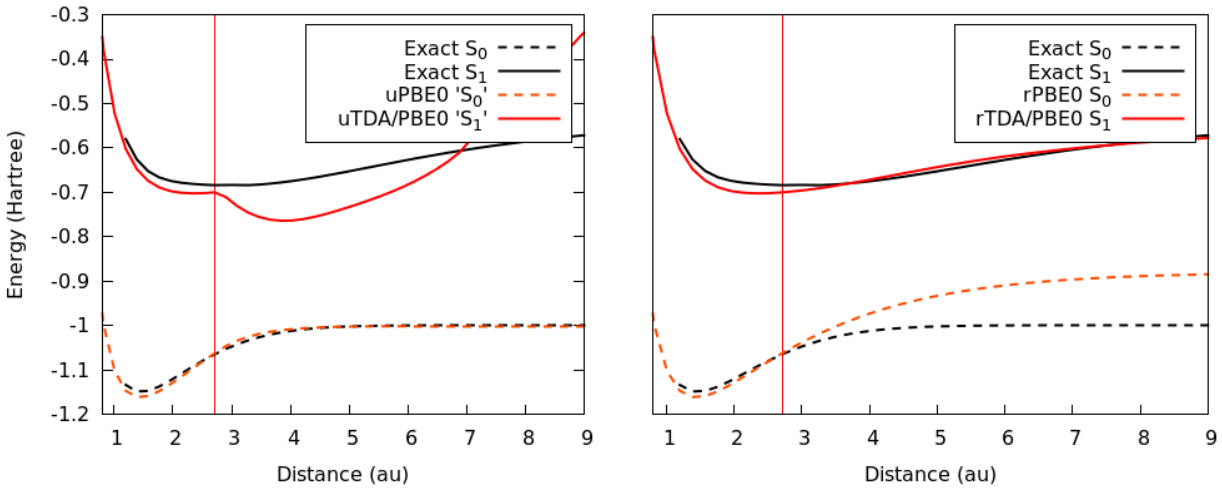

Figure 3.2: Left: Ground and excited state PESs for H_2 with UKS/PBE0 (red) with TDA unrestricted excitation and CCSD (black). The vertical line indicates the CF point. Beyond the CF the 'S_1' UKS/PBE0 state diverges significantly from the exact result. Right: Ground and excited state PESs for H_2 with RKS/PBE0 (red) with TDA and CCSD (black). The vertical line indicates the CF point. Beyond the CF the S_1 RKS/PBE0 state remains qualitatively similar to exact result.

the CF point. Additionally, uTDA/PBE0 and uTDA/PBE present a double minimum, the second of which occurs directly beyond the CF point.

Since it describes the ground state very well and reasonably well near the excited state equilibrium point, uTDA/PBE0 is used for the remainder of this chapter. However, due to the undesirable double minimum in the uTDA/PBE0 PES beyond the CF point, it remains to be tested how significant excited state artifacts might be: 1) If dynamics are dominated by ground state processes, then certainly uTDA/PBE0 is a reasonable method for computed PESs and their gradients. 2) If dynamics in the excited states are dominated by motion near the excited state minimum, then the double minimum character beyond the CF point will be irrelevant. The CF point is discussed further in the following section.

3.3 SCF Procedures

3.3.1 Identification of the Coulson-Fischer Point and the Triplet Instability

In the vicinity of the Coulson-Fischer (CF) point the PES becomes unstable. These instabilities are mitigated by a number of techniques discussed in the following sections. Here, the procedure for identifying the CF point is discussed. At each classical time step along a trajectory while the molecule is in a spin-restricted state, a stability analysis is performed. A stability analysis yields eigenvalue of the orbital rotation Hessian, considered here to be a "stability measure." When the stability measure becomes negative, a triplet instability[56] is identified, which occurs when the first triplet TDDFT excitation crosses zero. This is highlighted by Casida *et al.*[57] and, for time-dependent HF by Peach *et al.*[55], is illustrated in Fig. (3.3). Additionally, the stability parameter can be used to gauge proximity to the triplet instability, which as we will see is useful for developing an adaptive time-stepping scheme. The procedure for breaking spin-symmetry is shown in Algorithm 1. Next, currently available self-consistent field (SCF) procedures are discussed. Particularly, they do not properly break spin-symmetry at the CF point leading to energy conservation violation. CF point and triplet instability are used interchangeably in the rest of this chapter.

3.3.2 Failure to Break Spin-symmetry

Current SCF procedures[58] do not necessarily break spin-symmetry at the Coulson-Fischer point, even when UKS orbitals are used. This is illustrated in Fig. (3.4). In both the upper and lower panels of Fig. (3.4) H_2 trajectories are given the same total energy which is sufficient for bond dissociation ($E_{tot} > -1$ Hartree). However, unless spin-symmetry

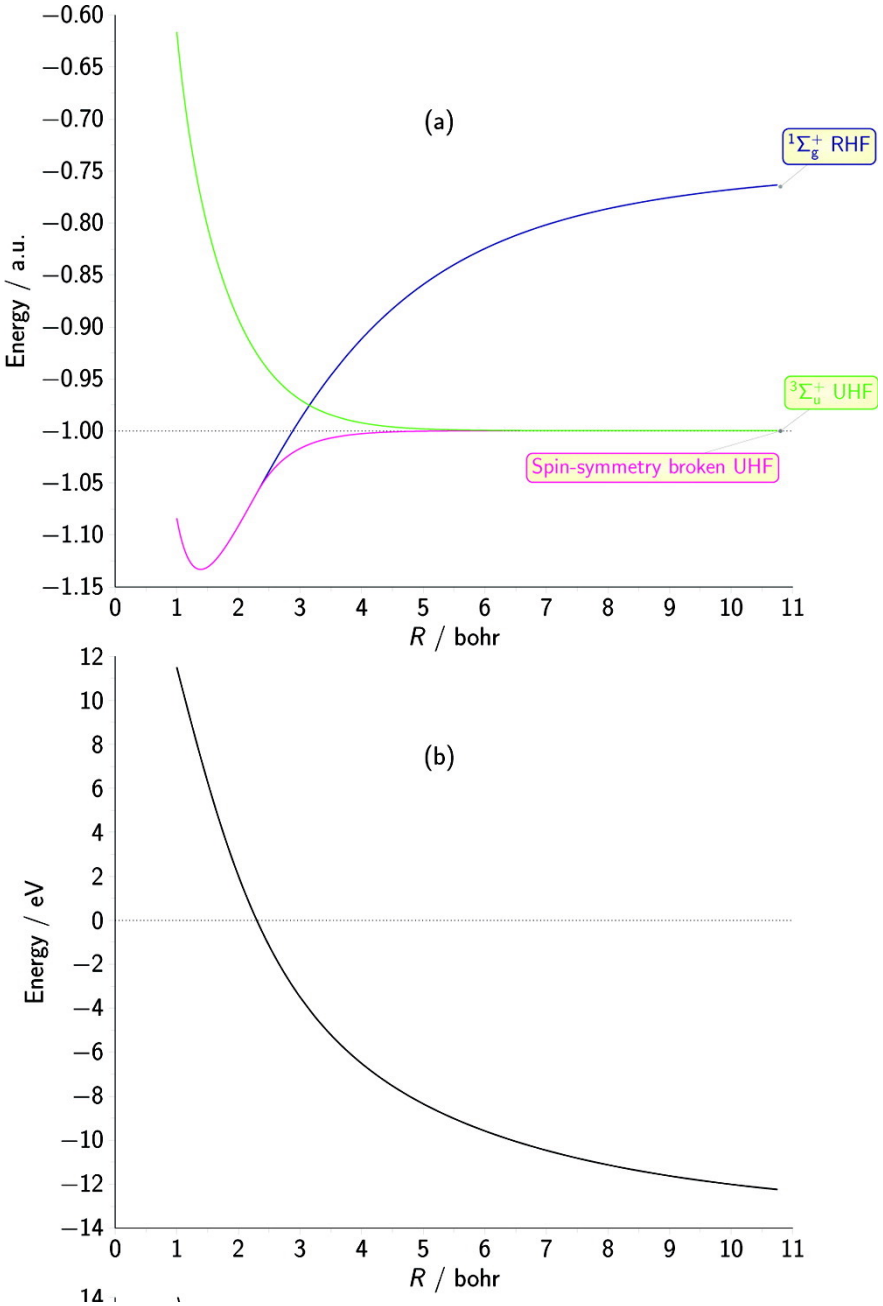

Figure 3.3: (a) Hartree-Fock (HF) electronic energy, and (b) HF triplet stability measure for H_2 as a function of bond length R, using the d-aug-cc-pVTZ basis set. A triplet instability occurs when the first TDHF triplet excitation is zero. Reprinted with permission from Ref.[55], Copyright 2011. American Chemical Society.

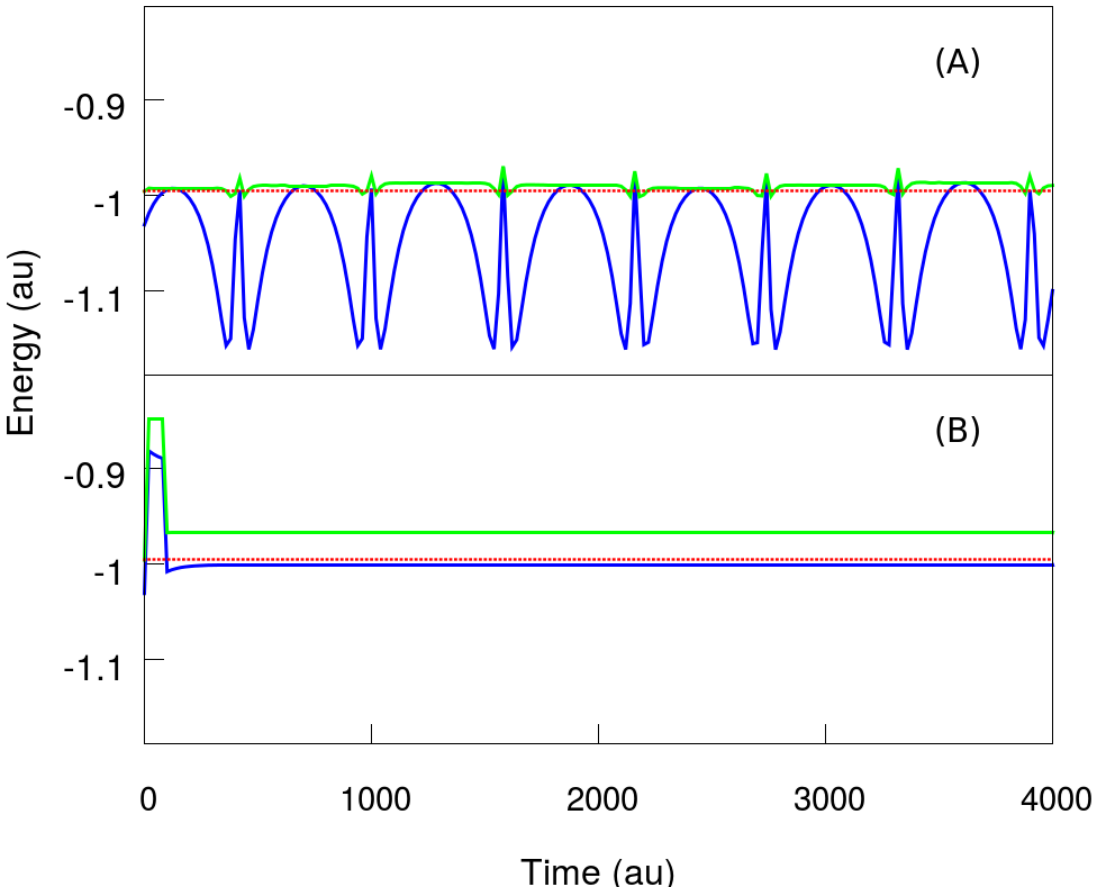

Figure 3.4: Comparison of H_2 trajectories with and without spin-symmetry breaking; both trajectories have identical initial conditions. Potential energy (blue) and total energy (green) are plotted versus time (au). Trajectory (A) does not undergo stability analysis and no spin-symmetry breaking is enforced; the trajectory does not dissociate. Trajectory (B) undergoes stability analysis at each step. This leads to identification of triplet instabilities, followed by forced spin-symmetry breaking. While this trajectory does dissociate, energy conservation is violated. UKS calculations are performed with def2-SV(P) basis[32], PBE0[54] exchange-correlation functional. Equations of motion integrated with the Leapfrog Verlet algorithm with constant time step of 20au.

breaking is explicitly enforced, as in panel (B), H_2 will not dissociate, as in panel (A). Failure to break spin-symmetry leads to unphysical bound states. Identification of the CF point and spin-symmetry breaking are implemented according to Algorithm (1).

while *spin-symmetry is not broken* **do**
  Perform stability analysis;
  if *Triplet instability* **then**
    1. Force UKS triplet occupation
    2. Perform SCF calculation
    3. Use converged triplet MOs as start MOs for SCF calculation with UKS singlet occupation
    if *Trajectory in excited state* **then**
      Proceed to excited state gradient calculation with new broken spin-symmetry reference
    else
      Proceed to ground state gradient calculation with new broken spin-symmetry reference
    end
  end
end

Algorithm 1: Algorithm for detection of Coulson-Fischer point and enforced spin-symmetry breaking. This algorithm is implemented in the trip_instab function of the v1.6_jobex script in a local working version of TURBOMOLE.

3.4 Adaptive Time Stepping

Energy conservation is volatile near the CF point and is sensitive to the classical integration time step chosen. Smaller integration time steps, as depicted in Fig. (3.5), improve energy conservation in dynamics calculations in general; however, when a triplet instability is not detected quick enough, there is an unphysical increase in the potential energy which occurs near the triplet instability. Therefore, energy conservation is violated when crossing a triplet instability. This is illustrated in Fig. (3.4). As demonstrated in panel (B), there is a sudden increase in the potential energy when the ground state switches from RKS to UKS MOs. While the PES shows good behavior well beyond the triplet instability, an increase in the kinetic energy occurs following the transition from RKS to UKS reference.

For simulating long trajectories, large classical integration time steps are desirable. In the adaptive time stepping scheme presented here, the time step is allowed to become large far from the CF point. As the trajectory approaches a triplet instability, the time step is scaled according to

$$\Delta t_i = \alpha\lambda, \tag{3.1}$$

where Δt_i is the current time step, α is the proportionality constant, which may be system dependent, and λ is the stability parameter. Energy conservation is the primary criterion for determining optimal integration time step scaling, in accordance with Eq. (3.1). The adaptive time stepping scheme developed is illustrated in Fig. (3.6), and implemented in Algorithms (2) and (3).

The specific time steps represented in Algorithm 2 (15au, 3au, and 30au) were empirically shown to improve energy conservation in acetaldehyde dynamics, which is further discussed in Chapter 4. In particular, it was found that the excited state PES was more

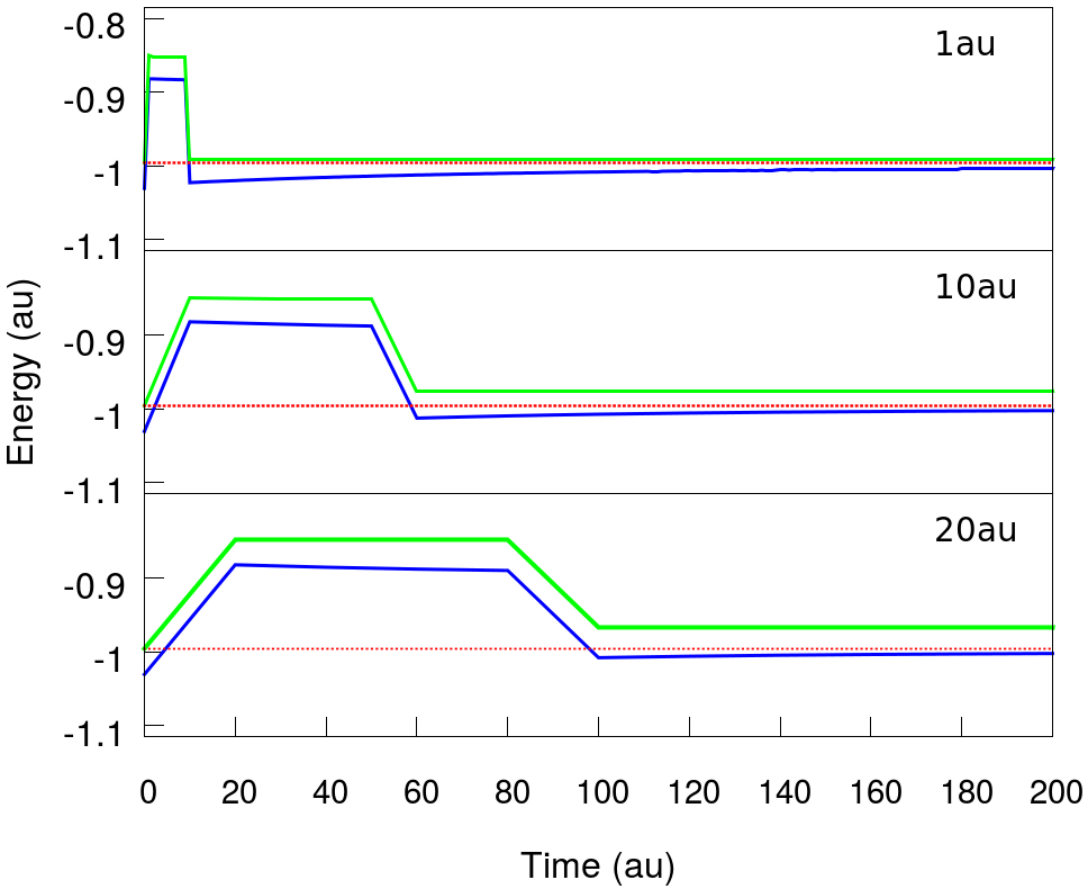

Figure 3.5: Three different time step scaling schemes for H_2 trajectories with identical initial conditions and default \$scfconv and \$denconv. Potential energy (green), total energy (blue), and initial total energy (dashed red) for H_2 trajectories with spin-symmetry breaking, with three different time step scaling schemes. In all three panels the potential energy jumps at the triplet instability, where $\langle S^2 \rangle = 1$, and then drops back to the expected PES when $\langle S^2 \rangle = 0.75$. Lower panel minimum time step is 20 au, middle panel time step scales to minimum 10au, and upper panel time step scales to minimum 1au. H_2 dissociates in all three trajectories. UKS (TD)DFT calculations performed with UKS (TD)DFT with PBE0 exchange-correlation functional in SV(P) basis. EOM integrated with Leapfrog Verlet[59] with variable time step scaling method.

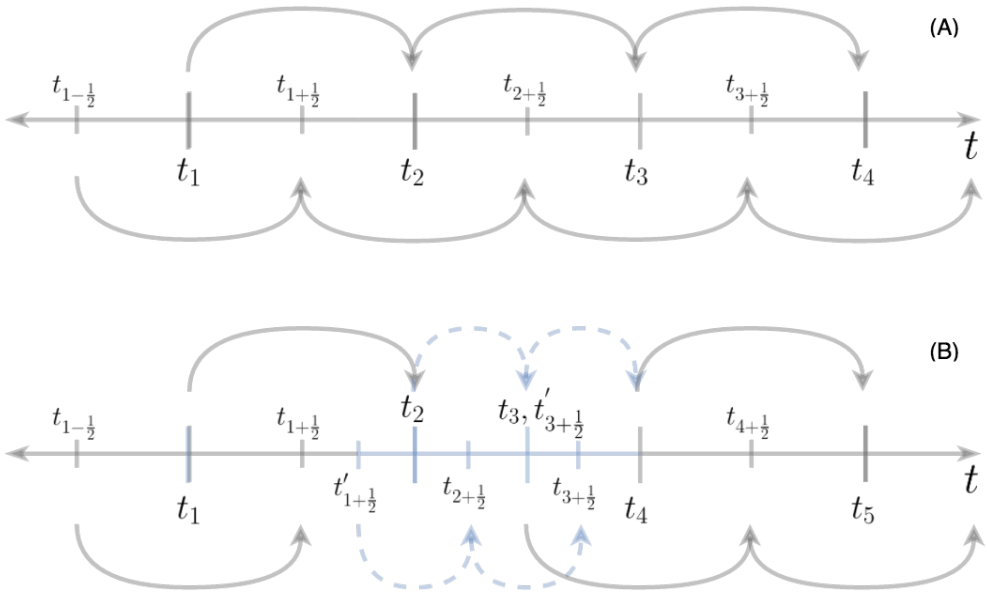

Figure 3.6: Schematic for Leapfrog Verlet algorithm (A) and for adjusted Leapfrog Verlet with scaled time steps (B). (A) shows typical progression for time and half-time steps with constant Δt. In schematic (B) when going from larger Δt (in gray) to smaller Δt (in blue) the half-time step is shifted forward in time so that $t_{i-\frac{1}{2}}$ is equidistant from $t_{i+\frac{1}{2}}$ where i indicates the current step. When going from smaller Δt to larger Δt (blue to gray) the half-time step is shifted backward in time so that $t_{i-\frac{1}{2}}$ is equidistant from $t_{i+\frac{1}{2}}$, where i indicates the current step.

if $\lambda < 0.015$ **then**
  if *Trajectory in excited state* **then**
    $\Delta t_{nextstep} = 3au$
    Set $scfconv = 1d-9 and $denconv = 1d-12
  else
    $\Delta t_{nextstep} = 15au$
  end
else
  if *Trajectory in ground state* **then**
    $\Delta t_{nextstep} = 3au$
    Set $scfconv = 1d-9 and $denconv = 1d-12
  else
    $\Delta t_{nextstep}$ = original time step
  end
end

Algorithm 2: Variable time step and convergence threshold scheme. λ is the stability parameter. This is implemented in the trip_instab function in the v1.6_jobex script in a local working version of TURBOMOLE.

for $i..N$ **do**
  if $\Delta t_{i-1} \neq \Delta t_i$ **then**
    $v_{i-\frac{1}{2}} = v_{i-\frac{1}{2}} + a_i \frac{1}{2}(\Delta t_{i-1} - \Delta t_i)$
  end
  else
    continue Leapfrog Verlet with constant Δt
  end
end

Algorithm 3: Time step scaling algorithm implemented leap.f in the froglib library of Turbomole. Refer to Fig. (3.6) for schematic of this algorithm. This is implemented in the leap.f subroutine in the frog library.

sensitive to the time step, and hence the smaller time step employed for excited state dynamics in Algorithm (2). Peach *et al.*[55] identify the relationship between the stability parameter and proximity to the triplet instability, shown in panel (b) of Fig. (3.3).

3.5 Sensitivity to Convergence Thresholds

At the CF point, the PES is sensitive to SCF and density convergence thresholds. This is illustrated for H_2 dynamics in Fig. (3.7). Remarkably, the delicacy of the PES near the CF point is coincident with an abrupt change in the character of the excited state (see Fig. (3.2)). To ensure energy conservation, tighter convergence thresholds are employed as a trajectory approaches a triplet instability, as shown in Algorithm (2)

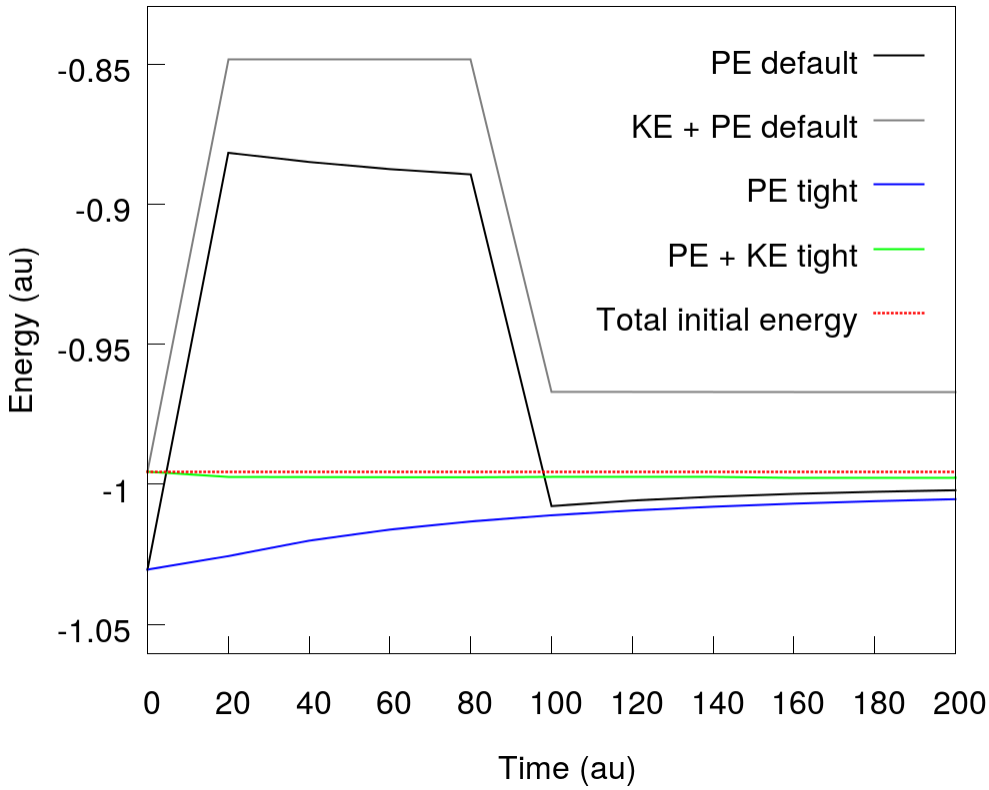

Figure 3.7: H_2 trajectories with constant time step and with spin-symmetry breaking. (A) the default SCF and density onvergence thresholds . Trajectory (B) is calculated with tighter convergence criteria. Both trajectories are integrated with 20au time step and given -0.9955 Hartree total initial energy for free dynamics. Only near the triplet instability are higher convergence thresholds required.

3.6 The Spin-symmetry Breaking Algorithm

The method for breaking spin-symmetry along *ab initio* dynamics trajectories is summarized in Fig. (3.8).

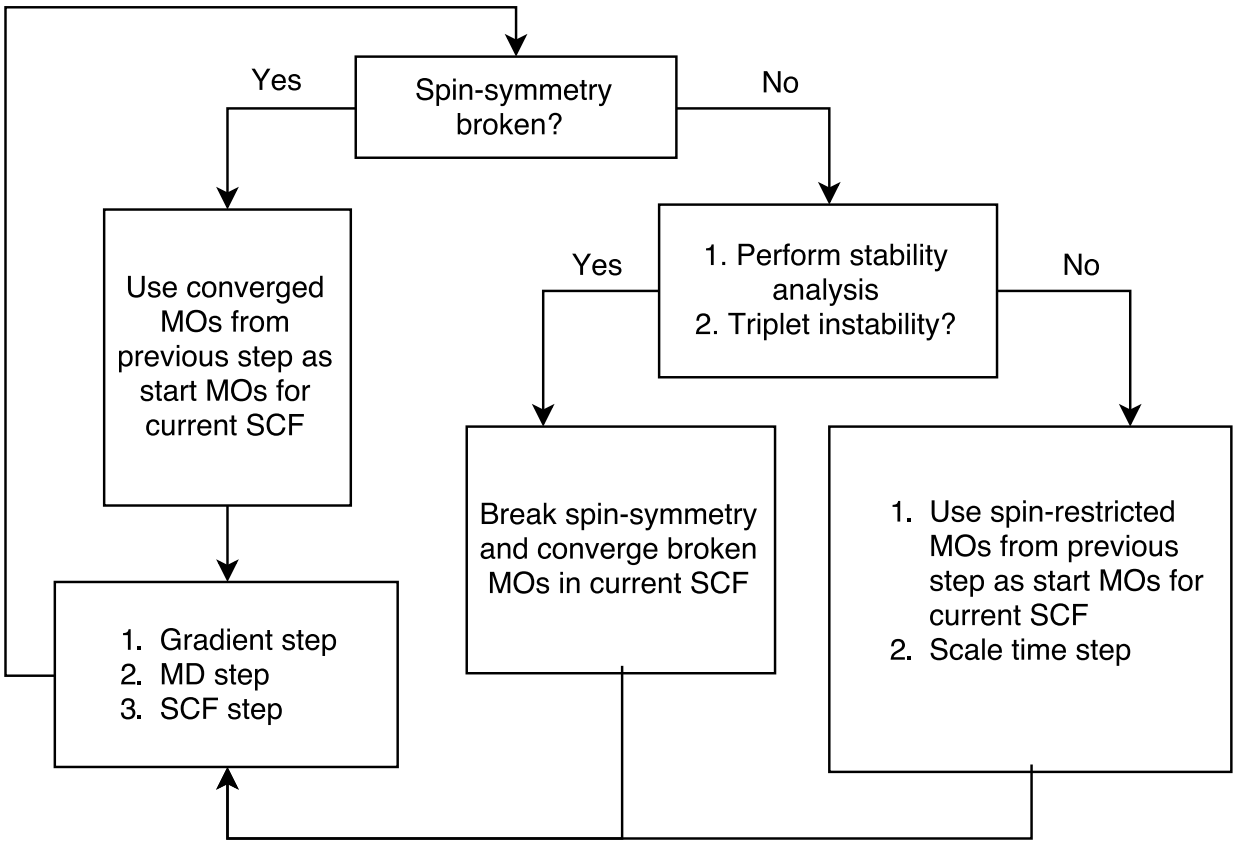

Figure 3.8: Implementation of a spin-symmetry breaking algorithm. Individual modules are elaborated upon in Algorithms 1 through 3. The trip_instab() function in the v1.6_jobex script performs stability analysis by calling define, dscf, and escf. Time steps are rescaled in the leap.f program in the froglib library in a local working version of Turbomole.

Chapter 4

Acetaldehyde Photodissociation Dynamics

Portions of this chapter from J.C. Vincent, M. Muuronen, K.C. Pearce, L.N. Mohanam, E. Tapavicza, and F. Furche, That Little Extra Kick: Non-adiabatic Effects in Acetaldehyde Photodissociation. Reproduced in part with permission from *Journal of Physical Chemistry Letters*, submitted for publication.

The material in this chapter is based upon work supported by the Department of Energy under Award DE-SC0008694 and the National Science Foundation under award CHE-0909227.

4.1 Introduction

Acetaldehyde is an abundant pollutant in the atmosphere[60,61] and serves as a model for carbonyl photochemistry[62]. Due to its small size and rich photochemistry as presented in the literature, acetaldehyde is an ideal computational benchmarking system. To describe the competing photochemical processes computationally, i.e. non-adiabatic transitions between excited states and breaking sigma-bonds both hetero- and homolytically, one has to account for spin-symmetry breaking in single reference methods. Therefore, the spin-symmetry breaking algorithm (SBA) with Tully-type surface hopping (SH-SBA) and the ground state Born-Oppenheimer SBA (BO-SBA), which were derived and implemented in Chapter 3, are evaluated here by application to acetaldehyde photochemistry.

Since 1933[63] acetaldehyde has been the subject of hundreds of studies, with many theoretical[64–72] and experimental[73–87] investigations occurring within the last two decades. Recently discovered roaming mechanisms[88–91] make acetaldehyde also an interesting molecule for exploring non-transition state (TS) dissociation mechanisms[25]. Several studies by Bowman *et al.* investigate roaming in acetaldehyde by simulating dynamics on a global S_0 potential energy surface (PES)[30,92–94]; they find that roaming constitutes the major mechanism forming CH_4 and CO when acetaldehyde is photoexcited between 308nm - 230nm. However, a number of questions still remain regarding acetaldehyde photodissociation dynamics: 1) How important are excited states for predicting accurate branching ratios, i.e. how does non-adiabatic molecular dynamics (NMD) compare to BO dynamics? 2) In surface hopping calculations, what role do non-adiabatic coupling vectors (NACV) play in dissociation mechanisms and branching? Lastly, 3) how well do single reference quantum chemical methods (DFT/TDDFT) describe radical intermediates and open-shell products?

To investigate these questions I simulated recent jet-cooled molecular beam experiments[95]

of acetaldehyde photoexcited at 157 nm are simulated using SH- and BO- SBA direct dynamics calculations. Branching ratios show qualitative agreement between experiment and both the SH- and BO-SBAs. However, divergence between the two methods is illustrated in dissociation mechanisms, and further with total kinetic energy (TKER) probability distributions, where SH-SBA improves the latter significantly. Furthermore, my results suggest BO simulation methods may overestimate the role of roaming dynamics in the formation of closed-shell CO + CH_4. Disparity between the TKER probability distributions, and a detailed examination of the role played by NACVs in dissociating trajectories, motivate a rationale for the divergence between the two methods. The improvements in the SH-SBA are proposed to arise from two main processes, which are depicted in Fig. (4.1): 1) Nuclear momentum is redistributed along NACVs into dissociating modes upon a surface hop from $S_1 \rightarrow S_0$; these are referred to as type-1 processes. 2) Excited state dynamics bias product formation by direct funneling of trajectories into dissociating regions of the ground state PES; these are referred to as type-2 processes. Lastly, two new concerted triple-fragmentation dissociation mechanisms are identified and discussed.

4.2 Computational Details

Ensembles with constant number, energy, and volume (NVE) of 440 SH-SBA and 400 BO-SBA direct dynamics simulations were performed. 71 SH-SBA and 211 BO-SBA trajectories violated energy conservation and are not considered in data analysis. Excited state PESs were computed using linear response time dependent density functional theory[14,37,50] within the Tamm-Dancoff Approximation (TDA)[41](LR-TDDFT-TDA). Known deficiencies associated with TDDFT PESs[96] near conical intersections were avoided by enforcing a surface hop from $S_1 \rightarrow S_0$ whenever the excitation energy was within 0.5 eV[4]. Unrestricted and restricted Kohn-Sham reference MOs were computed using the PBE0

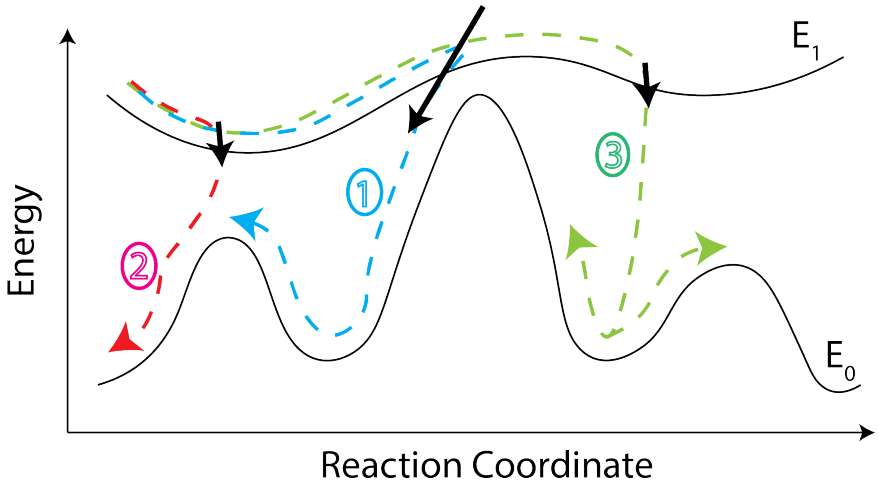

Figure 4.1: Three possible trajectory pathways coupling excited PES to ground PES in surface hopping dynamics: 1) Momentum rescaling along the non-adiabatic coupling vector upon a surface hop biases trajectory toward dissociation (type-1 process), 2) surface hop from $S_1 \rightarrow S_0$ directly into a dissociating region of the ground state PES (type-2 process) or 3) surface hop to a non-dissociating region of ground state PES, with subsequent dynamics similar to those of trajectories initialized in the ground state (type-3 process). The length of the bold black arrows represent the strength and direction of the non-adiabatic coupling vector.

exchange-correlation functional[33]. A Gaussian basis set implementation of DFT[58] and TDDFT[97] in Turbomole[5] was used. While smaller basis sets are known to blue-shift excitation spectra[4] good agreement existed between the def2-SV(P)[98] through def2-QZVPP[99] bases for the S_0 and S_1 PES gradients and thus def2-SV(P) basis set were employed. Non-adiabatic effects were simulated using an implementation of Tully's Fewest Switches Surface Hopping (FSSH) algorithm[15]. NACVs are computed using the implementation by Send and Furche[100]. Nuclear forces were computed from analytical ground state[101] and excited state gradients[102]. Classical nuclear equations of motion were integrated using an adaptive time stepping scheme which was described in Chapter 3, and is predicated upon the velocity Verlet[59] implementation in the FROG[103] module in Turbomole. Classical integration was performed over approximately 10,000 steps, resulting in total simulation times of approximately 4 ps.

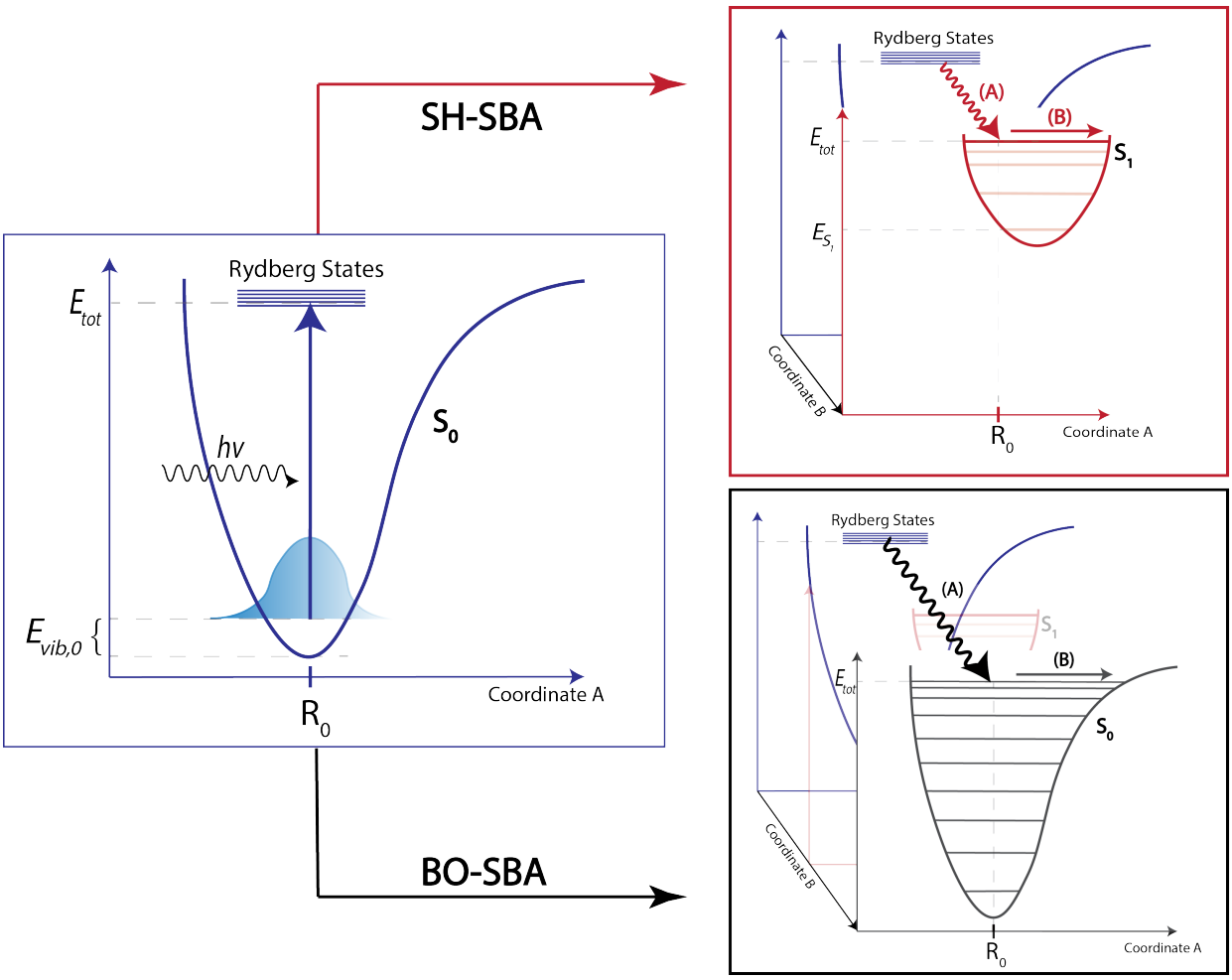

Figure 4.2: Schematic representation of initial conditions employed in the SH- and BO-SBA ensembles. **Left**: A vertical excitation into Rydberg states follows absorption of 157 nm light from the zero-point global S_0 minimum structure of acetaldehyde, denoted by R_0. $E_{vib,0}$ is the zero-point energy which is added to the excitation energy. **Upper right**: **(A)** Initial conditions for the SH-SBA ensemble. Ultra-fast internal conversion from Rydberg states to S_1 occurs in accordance with Kasha's rule. **(B)** After internal conversion into S_1 the trajectory begins to evolve in the excited state. **Lower right**: Initial conditions for BO-SBA ensemble. **(A)** Direct internal conversion from Rydberg states to high vibrational level of S_0 is assumed so that BO-SBA ensemble is initialized with total energy equivalent to the SH-SBA ensemble. **(B)** After internal conversion to S_0 the trajectory begins to evolve in the ground state. In both the lower left and right panels motion along a general second coordinate B is assumed to be negligible.

4.2.1 Initial Conditions

Prior to excitation, jet-cooled molecular beams[95] yield cold acetaldehyde molecules in their zero-point vibrational level. The single molecule zero-point energy (ZPE), $E_{vib,0} = 34.95$ kcal/mol, is computed within the harmonic approximation at the def2-SV(P)/PBE0 level. In the ZP vibrational level, the most probable geometry will be at the global PES minimum in the ground state, S_0. As depicted in Fig. (4.2), 157 nm (181.415 kcal/mol) light[95] incurs a vertical excitation from the ground state zero-point level to the Rydberg states. Subsequently, acetaldehyde is assumed to undergo ultra-fast internal conversion to S_1 (Kasha's rule[19]). Trajectory calculations are initialized in the S_1 excited state with a total kinetic energy, $KE^i_{S_1}$, corresponding to contribution from the photon, S_1 energy at the Franck-Condon point and the ZP energy in the ground state:

$$KE^i_{S_1} = E(157\text{nm}) + E_{vib,0} - E_{S_1}. \tag{4.1}$$

E_{S_1} is the potential energy of the S_1 state at the Franck-Condon point (101.552 kcal/mol). For comparison, BO-SBA trajectories are given a total energy equal to that of the SH-SBA trajectories (E_{tot} = 216.37 kcal/mol), which corresponds to the following initial kinetic energy in the ground state, KE_{S_0}:

$$KE^i_{S_0} = E(157\text{nm}) + E_{vib,0}. \tag{4.2}$$

Nuclear velocities are assigned randomly about a Gaussian distribution centered at $KE = \frac{1}{2}k_BT * DOF$ with variance $\sigma_i^2 = kT/m_i$, i.e. the velocity squared, v_i^2, for the ith atom. Here, KE is the initial kinetic energy of the trajectory, which is either $KE^i_{S_1}$ or $KE^i_{S_0}$, k_B is

Boltzmann's constant, T is the temperature and DOF is the internal degrees of freedom. Each atomic velocity is then scaled to ensure the total kinetic energy, KE, is fixed.

4.2.2 Constructing TKER Probability Distributions

TKER probability distributions, $P(E_t)$, for the H-loss channel were generated by: 1) Computing total translational kinetic energy, E_t, of momentum-matched products for each trajectory, and 2) binning the E_t to generate normalized distributions over a finite set of bins. E_t is computed as follows:

$$E_t = \frac{1}{2} m_{R_1} (1 + \frac{m_{R_1}}{m_{R_2}}) (\frac{d_{12}}{t})^2 \tag{4.3}$$

where m_{R_1} and m_{R_2} are the masses of momentum-matched products 1 and 2, respectively, d_{12} is the center-of-mass (COM) distance between products 1 and 2, and t is the time traveled in distance d_{12}. In units of kcal/mol, E_t values are discretized as follows:

$$E_t^l = 5(l-1) + 2.5, \quad \text{if} \quad -\frac{\Delta E_t}{2} < E_t - 5(l-1) + 2.5 < \frac{\Delta E_t}{2}, \tag{4.4}$$

where the index $l = \{1, .., 40\}$, and $\Delta E_t \equiv 5$kcal/mol is the bin size. The probability, P^l, that E_t is in bin, E_t^l, is given by

$$P^l = \frac{N_l^\gamma}{\alpha \sum_{j=1}^{40} N_j^\gamma}, \tag{4.5}$$

where γ refers to either H-loss or CH_3+CO channel, N_l^γ is the number of trajectories in bin E_t^l for dissociation channel γ, $\sum_{i=1}^{40} N_i^\gamma$ is the total number trajectories which dissociate along channel γ, and $\alpha = \Delta E_t$ is the normalization constant so that

$$\sum_{l=1}^{40} P^l \Delta E_t = 1. \tag{4.6}$$

Smooth approximate probability distributions of the discrete pairs (E_t^l,P^l) were generated using *acsplines* in Gnuplot 4.6[104].

4.2.3 Calculating Branching Ratios

Dissociation is defined as having occurred when a minimum bond length of 6Å exists between any two nuclei, at which point a simulation resulting in total simulation time less than 4 ps. Branching ratios, ϕ^γ, along dissociation pathway γ is computed as follows:

$$\phi^\gamma = \frac{N_i^\gamma}{\sum_{j=1}^{40} N_j^\gamma}. \tag{4.7}$$

We developed a screening tool which determined product formation based upon an interatomic distance metric; scans over hundreds trajectory files efficiently counted product formation.

4.2.4 Calculating Approximate Rotational and Vibrational Quantum Numbers

Rotational quantum numbers, J, and vibrational quantum numbers, ν, are computed for CO dissociation fragments. These quantum numbers are approximated from classical nuclei by binning the classical counterparts. The rotational energy levels are determined as follows: The classical rotational kinetic energy, KE_{rot}^{class} is computed,

$$KE_{rot}^{class} = \frac{1}{2}\boldsymbol{L}\boldsymbol{I}\boldsymbol{L}, \tag{4.8}$$

where $\boldsymbol{L}$ is the angular momentum, and $\boldsymbol{I}$ is the moment of inertia tensor. KE_{rot}^{class} is computed over several classical integration steps and then averaged and set equal to the quantum rotational energy for a diatomic,

$$\langle KE \rangle_{rot}^{class} = \frac{J(J+1)}{2I}, \tag{4.9}$$

where $I = \mu r^2$ is the moment of inertia for a diatomic with reduced mass μ and r is the CO bond distance. Eq. (4.9) is solved for rotational quantum number J and then rounded to the nearest whole number. In a similar manner the vibrational quantum numbers for CO, ν, are computed. The classical vibrational energy in a harmonic potential is set equal to the quantum harmonic oscillator energy:

$$E_{vib}^{class} = \frac{1}{2}\frac{\partial^2 U}{\partial r^2}(r_{max}^2), \tag{4.10}$$

$$= \frac{1}{2}k(r_{max}^2), \tag{4.11}$$

$$= \hbar(\nu + \frac{1}{2})\sqrt{\frac{k}{\mu}}. \tag{4.12}$$

r_{max} is the bond length at the classical turning point, and the force constant, k, is computed from the potential energy surface (at the global minimum). The quantum number, ν, is rounded to the nearest whole number.

4.2.5 Calculating the Period of Rotation

Triple-fragmentation dissociations of the type,

$$\mathrm{ABC} + h\nu \xrightarrow{t_0} \mathrm{ABC}^* \xrightarrow{t_1} \mathrm{AB}^* + \mathrm{C} \xrightarrow{t_2} \mathrm{A} + \mathrm{B} + \mathrm{C}, \tag{4.13}$$

are defined as synchronous concerted, asynchronous concerted, or step-wise by the following criteria[105]:

$$\frac{t_2 - t_1}{\tau_{rot}} = \begin{cases} 0 & \text{,then synchronous concerted,} \\ \leq 1 & \text{,then asynchronous concerted,} \\ \geq 1 & \text{,then step-wise.} \end{cases}$$

Above, $\tau_{rot} = 2\pi\omega^{-1}$ (where ω is the rotational velocity) is the rotational period of AB^*, and t_1 and t_2 are the times at which the second two dissociation steps in Eq. (4.13) occur. For analysis, t_1 and t_2 are measured directly by tracking the time step at which dissociation 1 and 2 occur, respectively.

The period of rotation is computed as follows: 1) The principle axes of rotation, $\{\boldsymbol{U}_\alpha, \boldsymbol{U}_\beta, \boldsymbol{U}_\gamma\}$, and principle moments of inertia, $\{I_\alpha, I_\beta, I_\gamma\}$ are determined as the eigenvectors and eigen-

values, respectively, of the moment of inertia tensor, $\boldsymbol{I}$,

$$\boldsymbol{I}\boldsymbol{U} = \begin{pmatrix} I_\alpha & 0 & 0 \\ 0 & I_\beta & 0 \\ 0 & 0 & I_\gamma \end{pmatrix} \boldsymbol{U} \tag{4.14}$$

where

$$\boldsymbol{U} = (\boldsymbol{u}_\alpha, \boldsymbol{u}_\beta, \boldsymbol{u}_\gamma). \tag{4.15}$$

Here the bold elements of $\boldsymbol{U}$ represent column vectors containing the vector coordinates for each of the respective principle axes. 2) The projection of the total angular momentum vector, $\boldsymbol{L} = \{L_x, L_y, L_z\}$ (which is centered about the center-of-mass, COM), about each principle axis, $\xi = \{\alpha, \beta, \gamma\}$, is

$$L_\xi = \frac{\boldsymbol{L} \cdot \boldsymbol{u}_\xi}{\boldsymbol{u}_\xi^T \cdot \boldsymbol{u}_\xi}. \tag{4.16}$$

3) The rotational velocity about principle axis ξ, ω_ξ, is then computed as

$$\omega_\xi = L_\xi / I_\alpha, \tag{4.17}$$

and finally, 4) the period of rotation is computed:

$$\tau_\xi = 2\pi\omega_\xi^{-1}. \tag{4.18}$$

4.3 Results and Discussion

Lee[95] observes nine dissociation channels listed in Table (4.1). These same dissociation channels were observed in my simulations. In particular, channels (2) and (6) are observed to branch along differing mechanisms when simulated with the SH- or BO-SBA. A brief analysis of branching ratios will be followed by an in-depth examination of the mechanisms for channels (2) and (6). The reader is referred to several studies investigating channels (1),(3),(4), and (5) through (9)[30,64–72,92–94].

4.3.1 Branching Ratios

Dissociation channel	SH-SBA	BO-SBA	Experiment
(1) CH_3 CO + H	0.03	0.06	0.01
(2) CH_3 + CO + H	0.37	0.62	0.50
(3) CH_2 CO + H + H	0.05	0.05	0.24
(4) CH_2 CO + H_2	0.03	0.10	0.14
(5) CH_3 + CHO			
(6) CH_4 + CO			
(7) CH_2 + CH_2O	0.09	0.09	0.10
(8) CH_2CH + OH			
(9) CHCH + H_2O			
No dissociation	0.44	0.08	

Table 4.1: SH-SBA and BO-SBA raw branching ratios for nine dissociation pathways in acetaldehyde at 157 nm. Empirical branching ratios are also reported from Lee[95]. Raw values are calculated from trajectories which dissociated within the 10,000 classical integration steps.

Table (4.1) shows qualitative agreement between the SH- and BO-SBA calculations and the molecular beam experiments of Lee[95]; small discrepancies between the methods are discussed here. 44% of the SH-SBA and 8% of the BO-SBA trajectories did not dissociate within the 10,000 integration steps. The large difference in non-dissociating branching ratios indicates SH-SBA calculations increase the lifetime of acetaldehyde compared to BO-SBA. This result is expected due to sequestration of internal energy into electronic potential energy in the excited state, which occurs only for trajectories in the SH-SBA simulations.

For channel (1), Lee[95] observes that the dominant contribution to single H-loss is due to hot dissociation along the first triplet state. This observation is consistent with my results: Internal energy calculations of almost all CH_3CO fragments indicates there is sufficient energy in vibrational modes to overcome the CC bond dissociation barrier of 26.4 kcal/mol. Therefore, given additional simulation time both SBAs are expected to yield a branching ratio of zero for channel (1). Furthermore, since the triplet state is not explicitly computed in the SBAs, low yield along triplet state dissociations is expected. Along channel (3), both the SBAs exhibit relatively low yields. This may also be due to the missing triplet state dynamics, and may explain why this and channel (1) both have low calculated yields. Lastly, the disparity in branching between the SH- and BO-SBA along channel (4) is not entirely clear. It may also be due to undissociated trajectories in the SH-SBA. Though low yield along channel (4) was also observed in ground state calculations by Han *et al.*[94], albeit at lower excitation energy of 308nm.

For both the SH- and BO-SBA channel (2) dominates all others, which is consistent with the experiment[95]. However, the BO-SBA branches considerably more along channel (2) than does SH-SBA. Since branching is relatively consistent between the SH- and BO-SBA along all the other channels it is hypothesized that the low branching along channel (2) in SH-SBA is largely due to undissociated trajectories.

4.3.2 Mechanisms: SH-SBA vs BO-SBA

While branching ratios show qualitative agreement between both the SH- and BO-SBA and experiment, mechanisms show notable differences between the two methods. In particular, the roaming formation of CH_4 and CO, and two new concerted triple-fragmentation dissociations to products CH_3, CO, and H are analyzed below.

Roaming

As illustrated in Fig. (4.3), "Roaming" occurs when CH_3CHO dissociates homolytically along the C-C bond creating CH_3 and CO intermediates. Following homolytic bond cleavage, a period of approximately 150fs passes where the CH_3 and CHO intermediates "roam" about the other. Then, the CH_3 fragment abstracts the hydrogen from the CHO fragment and subsequently forms vibrationally hot CH_4 and rotationally cold CO. At the point of H-abstraction the C-C bond distance is 3.4 Å, which is consistent with calculations by Shepler *et al*[93]. A similar mechanism has been observed in previous studies by Houston and Kable[88], Heazlewood *et al.*[30], and Rubio-Lago *et al.*[90,91]. The roaming mechanism is observed in the CH_4+CO channel in both the BO-SBA and SH-SBA ensembles, and an example trajectory is depicted in Fig. (4.3).

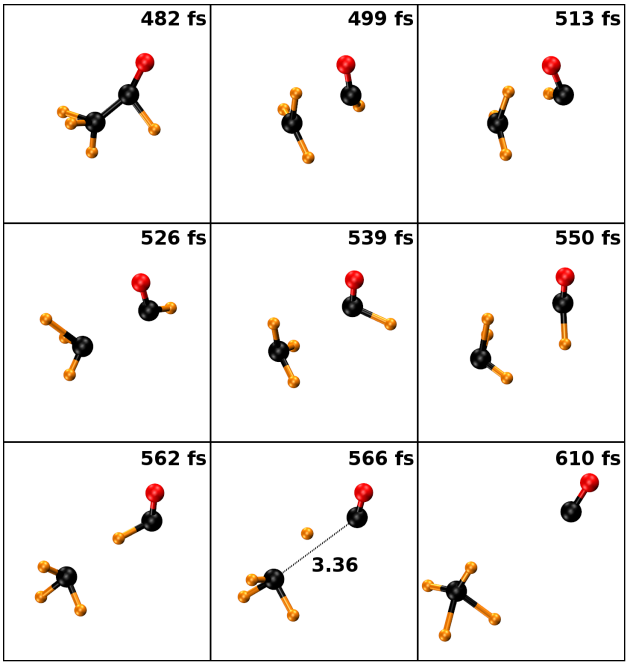

Figure 4.3: Example BO-SBA trajectory dissociating to products CH_4+CO via a roaming mechanism. The CH_3+ CHO fragment at 499 fs followed by H-abstraction at 566 fs. C-C bond distance at H-abstraction is 3.36 Å.

	SH-SBA			BO-SBA		
	J	ν	E_t	J	ν	E_t
Mean	47.09	1.27	28.37	34	0.14	25.92
Std Dev	11.58	1.10	8.83	14.74	0.40	18.66
Spread	39	3	29.67	38	1	44.93

Table 4.2: Mean, standard deviation, and distribution spread for rotational and vibrational quantum number for CO in CH_4+CO channel for the SH-SBA and BO-SBA. There are 11 data points for SH-SBA adn 7 data points for the BO-SBA. The E_t are in unites of kcal/mol.

In the SH-SBA ensemble 11 trajectories dissociated along the CH_4+CO channel, and of those only two dissociated via a roaming mechanism. Dissociation along this pathway occurs immediately after the trajectory hop from $S_1 \rightarrow S_0$, within an average of 2.25 fs (σ =0.9 fs) since a hop. For the BO-SBA 7 trajectories dissociated along the CH_4+CO channel where all but 2 dissociated via a roaming mechanism. Table 4.2 displays the

mean, standard deviation, and spread of the rotational and vibrational quantum numbers for the CO fragment for both SH-SBA and BO-SBA. The SH-SBA CO products have an average rotational and vibrational constant of 47.09 and 1.27, respectively, with a maximum vibrational level of ν =3 while BO-SBA has relatively cold rotational and vibrational constants of 34 and 0.14, respectively, with a maximum ν =1. Roaming is the dominant mechanism for methane formation in the BO-SBA, consistent with the prevailing interpretation in previous experiments and ground state computational observations[30,88,93]. However, the hot rotational and vibrational signatures in my SH-SBA simulations, in addition to the immediate dissociation along this channel following a surface hop, suggest that excited state dynamics may play an important role in suppressing the roaming channel.

Concerted Triple-Fragmentation

The triple-fragmentation dissociation, channel (2), dominates all others with 37% and 62% of all SH- and BO-SBA trajectories, respectively, dissociating through it. This observation is in qualitative agreement with Lee's molecular beam experiments[95] and calculations by Han *et al.*[94]. These triple-fragmentations were observed to occur through three distinct dissociation pathways:

$$CH_3CHO + h\nu \xrightarrow{t_0} CH_3CHO^* \xrightarrow{t_1} CH_3CO^* + H \xrightarrow{t_2} CH_3 + CO + H, \tag{4.19}$$

$$\xrightarrow{t_1} {CH_4}^* + CO \xrightarrow{t_2} CH_3 + CO + H, \tag{4.20}$$

and

$$\xrightarrow{t_1} CHO^* + CH_3 \xrightarrow{t_2} CH_3 + CO + H. \tag{4.21}$$

Reaction 4.19 representing primary dissociation through homolytic C-H bond (96kcal/mol) cleavage, is the most prevalent one for the limited simulation times studied here. An approximately equal amount of dissociations of reaction type 4.21 are possible. Due to the longer simulation times required to break the C-C bond (100kcal/mol) in the formation of CH_3 and CHO (Equation 4.21), secondary CHO$\rightarrow$H+CO formation was limited by the 10,000 time steps simulated here. Additionally, reaction 4.21 is known to occur primarily through a dissociative T_1 pathway[94], as discussed in Section 4.3.1. The minor reaction 4.20 is observed solely in the BO-SBA simulations, and has been observed by Han *et al.*[94]; the reader is referred there for further discussion on this pathway. Thus, only triple-fragmentation dissociations in reaction 4.19 are further considered below.

Lee[95] suggests the primary mechanism producing triple-fragmentations are sequential. However, 42% of the BO-SBA and 35% of SH-SBA dissociate through either a synchronous or an asynchronous concerted mechanism. An example trajectory of the synchronous concerted dissociation pathway in acetaldehyde is shown in Fig. (4.4).

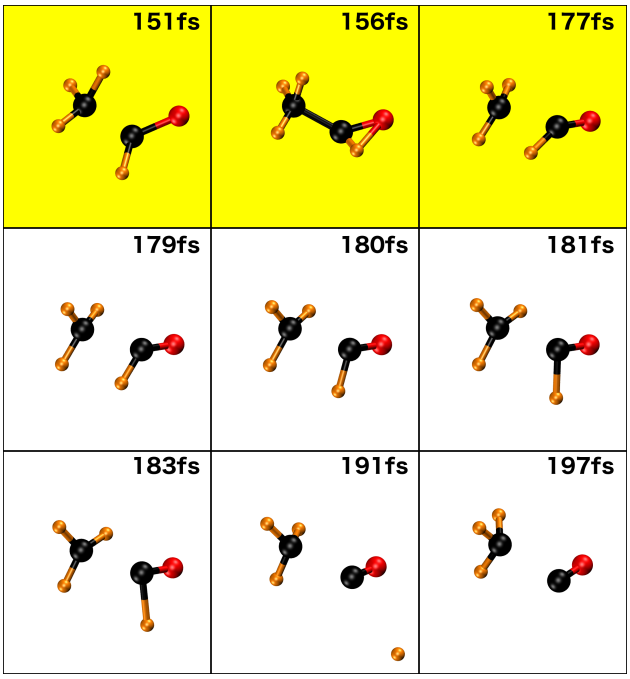

Figure 4.4: Concerted tertiary dissociation of acetaldehyde to H + CO + CH_3. Yellow background indicates trajectory is in excited S_1 state, and white indicates trajectory is in S_0 ground state.

Table 4.3 shows the fraction of triple-fragmentation dissociations which occur through synchronous and asynchronous concerted mechanisms, as well as the average minimal period of rotation for the CH_3CO^* intermediate. 23% and 19% of BO-SBA dissocations occur through synchronous and asynchronous mechanisms, respectively. This diverges from the 3.5% and 32% of the respective dissociations in the SH-SBA simulations. One reason for the differences between the two methods is the higher rotational frequencies of the CH_3CO intermediates in the SH-SBA simulations, effectively driving the defining $(t_2\text{-}t_1)/(\tau_{min})$ ratio toward larger values. This effect is later rationalized as a direct result of energy redistribution along the NACV.

	BO-SBA			SH-SBA		
	f	$\langle\tau_{min}\rangle$	σ	f	$\langle\tau_{min}\rangle$	σ
Synchronous	0.23	2	3	0.035	0.15	0.20
Asychronous	0.19	0.15	0.2	0.32	0.15	0.18
Step-wise	0.58	0.10	0.08	0.65	0.04	0.04

Table 4.3: Synchronous, asynchronous, or step-wise concerted dissociations of type Equation 4.19. f is the fraction of trajectories dissociating along $CH_3CO \rightarrow CO{+}CH_3$ with either synchronous or asynchronous concerted or step-wise dissociations, $\langle\tau_{min}\rangle$ is the mean of the minimal period of rotation for CH_3CO about its principal rotation axes in picoseconds, and σ is the standard deviation of the τ_{min} distribution in picoseconds.

4.3.3 TKER Probability Distributions

SH- and BO-SBA provide differenct mechanisms. To understand and justify the correct mechanism, we can further compare TKER probability distributions of the selected pathways to experimental values.

H-loss Channels

Several primary and secondary dissociation processes account for the channel (1) TKER probability distributions depicted in Fig. (4.5):

Primary

$$CH_3CHO \rightarrow H + CH_3CO \tag{4.22}$$

$$\rightarrow H + CH_3 + CO \tag{4.23}$$

Secondary

$$CH_3CO \rightarrow H + CH_2CO \tag{4.24}$$

$$HCO \rightarrow H + CO \tag{4.25}$$

$$CH_4 \rightarrow H + CH_3 \tag{4.26}$$

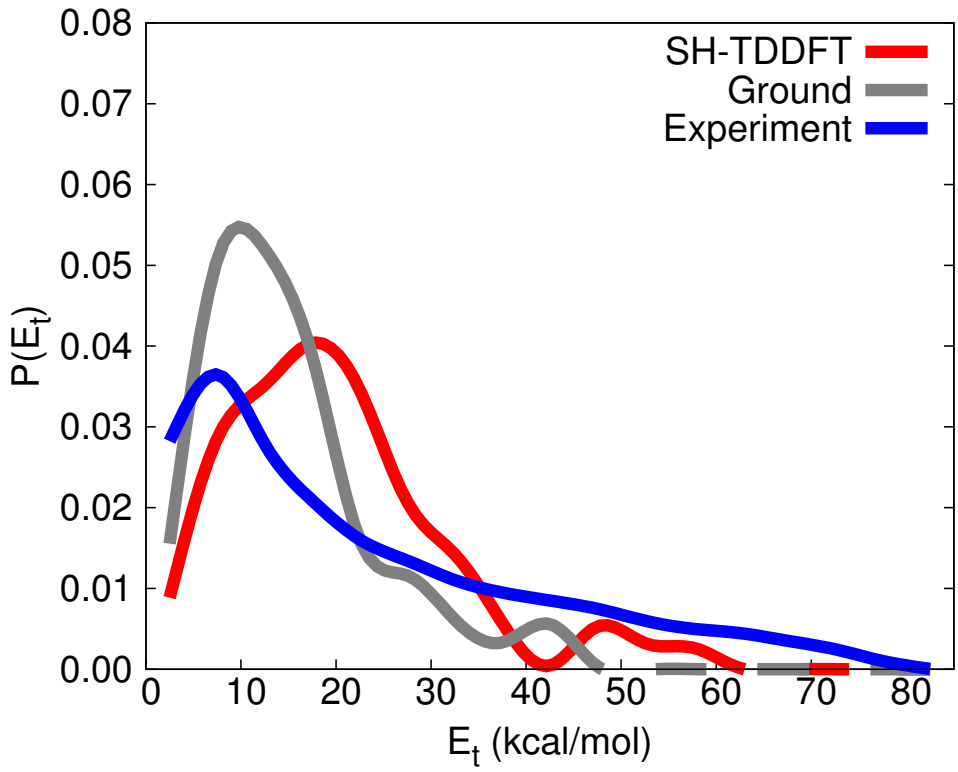

Figure 4.5: H-loss channel TKER probability distributions for experiment[95] (blue), SH-SBA (red), and BO-SBA (gray). Distributions are computed from 166 SH-SBA and 151 BO-SBA trajectories which dissociated along the H-loss channels.

Averages, standard deviations, and the mode for the distributions plotted in Fig. (4.5) are given in Table (4.4). The mode of the BO-SBA distribution is shifted by approximately +4 kcal/mol with respect to the experimental distribution, while the SH-SBA is shifted by +11 kcal/mol. With respect to the mode, the BO-SBA gives a result in closer accord with the experimental value. The SH-SBA has an average E_t ≈20 kcal/mol which is shifted by

-3 kcal/mol with respect to the experimental value, while the average E_t for the BO-SBA is approximately 15 kcal/mol which is shiftedby 8 kcal/mol. The spread in the SH-SBA distribution is approximately 11.5 kcal/mol, which is less than that of the experiment by about 7 kcal/mol, whereas the BO-SBA is 9.5 kcal/mol less than that of the experiment. In both the average and the spread of the distributions SH-SBA gives a result in closer accord with the experimental distribution than does the BO-SBA.

Table 4.4: Mean, standard deviation, and mode for SH-SBA, BO-SBA, and experiment TKER probability distributions for the H-loss channel. All numbers are in units of kcal/-mol.

	$\langle E_t \rangle$	σ	mode
Experiment	23.02	18.67	7.5
SH-SBA	20.03	11.47	17.5
BO-SBA	15.00	9.09	12.5

The BO-SBA TKER probability distributions, depicted in Fig. (4.5) and (**??**), are strongly peaked about the mode with a relatively small standard deviation. This is in contrast to the SH-SBA distributions, which show a broadening of the TKER energies. Additionally, the SH-SBA distributions better simulate the molecular beam distributions. These results suggest that the excited state dynamics play a pivotal role in the redistribution of internal energy in the ground state, which effectively spreads out the distributions in the SH-SBA.

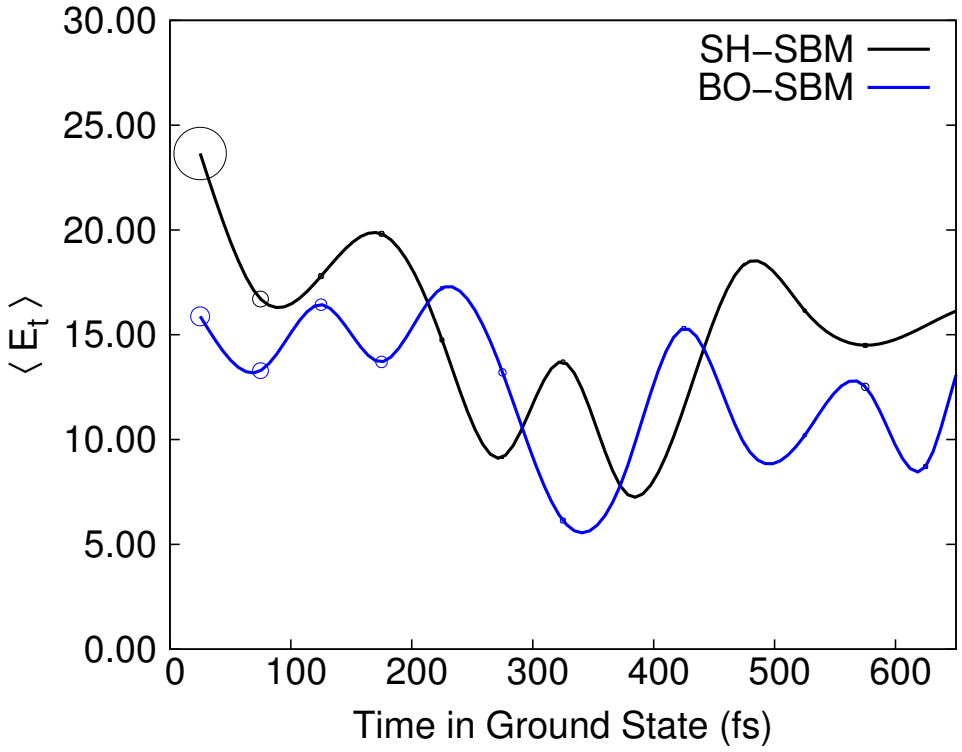

Figure 4.6: Expected TKER versus integration time step for the H-loss channel. Upon a surface hop, the SH-SBA trajectories (black) commence integration in the ground state. The radius of the circles are directly proportional to the frequency with which trajectories dissociate at that step. The maximum expected E_t occurs immediately after a surface hop, within 50 fs. The BO-SBA (blue) curve provides a background reference for expected TKER.

Type-1 processes, depicted in Fig. (4.1), provide a rationale for this redistribution of kinetic energy: Hot dissociation occurs via direct transfer of excited state potential energy into dissociating modes. This happens when the NACV has a large projection along the dissociating mode. This effect is demonstrated in Fig. (4.6), where high energy H-loss is shown to occur most frequently within 50 fs following a surface hop. An example of an H-loss dissociation occurring along the NACV is shown in Fig. (4.7). It is clear that upon a surface hop, the subsequent H-loss occurs along the NACV. This is contrasted with the BO-SBA background where there is no clear biasing of H-loss TKER with respect to the integration time-step. This is remarkable as it shows direct evidence of the influence of the

surface hop on dissociation TKER, and explains why the distributions in Fig. (4.5) and (**??**) tend toward higher average TKER and standard deviations in the SH-BOA simulations.

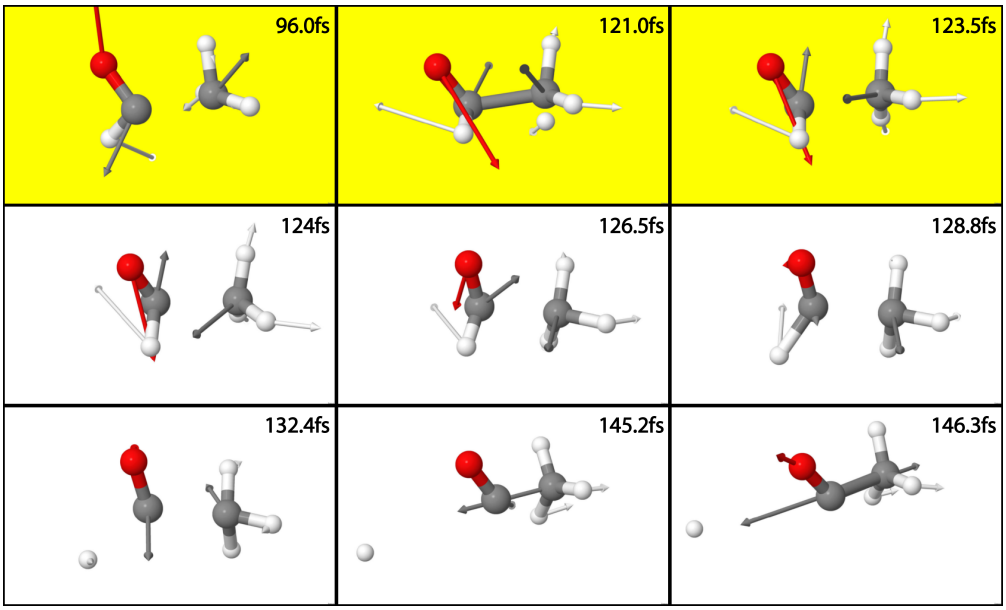

Figure 4.7: The influence of the NACV on surface hopping trajectories. H-loss dissociates along the NACV following a surface hop from S_1 (yellow) to S_0 (white).

4.4 Conclusions

Molecular beam experiments of acetaldehyde photoexcited with 157 nm light were simulated using the SH- and BO-SBAs. All nine dissociation channels were observed, and branching ratios for both the SH- and BO-SBAs were in qualitative agreement with experiment. However, discrepancy between the SH- and BO-SBA are indicated in analysis of mechanisms and TKER probability distributions. In particular, the formation of CH_4 is found to follow roaming-type dissociation predominately in the BO-SBA simulations whereas in the SH-SBA it follows a tight TS dissociation mechanism. Furthermore, the NACVs play a critical role in non-adiabatic dynamics. This influence of the NACVs is rationalized as a manifestation of the type-1 process depicted in Fig. (4.1). Finally, two new concerted triple-fragmentation dissociations to products $H+CO+CH_3$ were identified.

Notably, the SH-SBA and BO-SBA give near equal amounts of concerted fragmentations, however the former shows a suppression of the synchronous concerted dissociation due to faster rotational velocities of the excited intermediate. It is proposed that further divergences between non-adiabatic and BO dynamics will occur due to type-2 processes, suggesting once again the importance of non-adiabatic effects for predicting branching and mechanisms in photodissociation processes.

Chapter 5

Outlook

For the first time ever homolytic bond cleavage events are now described using single reference density functional surface hopping methods with the spin-symmetry breaking algorithm developed in this thesis. Although homolytic bond cleavage has been simulated with promising results there are still a number of challenges for this project going forward. Nearly half of the BO-SBA simulations resulted in a violation of energy conservation and were thus not included in the above analyses. The causes of these violations should be further investigated so as to produce a more robust method with nominal losses. Benchmark studies on acetaldehyde show that this method yields semi-quantitative accuracy when compared to experiments, which is encouraging. Finally, since density functional methods scale well with system size it is now feasable to model photochemistry of large systems (> 100 atoms) at reasonable cost.

Bibliography

[1] N. J. Turro, V. Ramamurthy, and J. C. Scaiano, *Modern molecular photochemistry of organic molecules* (University Science Books, 2010).

[2] B. J. Finlayson-Pitts and J. Pitts, *Chemistry of the Upper and Lower Atmosphere* (Academic Press, San Diego, 2000).

[3] S. Tan, H. Feng, Y. Ji, Y. Wang, J. Zhao, A. Zhao, B. Wang, Y. Luo, J. Yang, and J. G. Hou, J. Am. Chem. Soc. **134**, 9978 (2012).

[4] E. Tapavicza, A. M. Meyer, and F. Furche, Phys. Chem. Chem. Phys. **13**, 20986 (2011).

[5] F. Furche, R. Ahlrichs, C. Hättig, W. Klopper, M. Sierka, and F. Weigend, WIREs Comput. Mol. Sci. **4**, 91 (2014).

[6] A. J. Cohen, P. Mori-Sanchez, and W. Yang, Science **321**, 792 (2008).

[7] J. J. Szymczak, M. Barbatti, and H. Lischka, Int. J. Quantum Chem. **111**, 3307 (2011).

[8] S. Faraji, M. Vazdar, V. S. Reddy, M. Eckert-Maksic, H. Lischka, and H. Koppel, J. Chem. Phys. **135**, 154310 (2011).

[9] F. Plasser, R. Crespo-Otero, M. Pederzoli, J. Pittner, H. Lischka, and M. Barbatti, J. Chem. Theory Comput. **10**, 1395 (2014).

[10] S. Grimme, Anger. Chem. Int. Ed. Engl. **52**, 6306 (2013).

[11] W. Domcke, D. R. Yarkony, and H. Koppel, eds., *Conical Intersections: Electronic Structure, Dynamics and Spectroscopy*, Vol. 15 (World Scientific, Singapore, 2004).

[12] A. Szabó and N. S. Ostlund, *Modern quantum chemistry : introduction to advanced electronic structure theory* (Dover Publications, Mineola (N.Y.), 1996).

[13] W. Koch and M. C. Holthausen, *A Chemist's Guide to Density Functional Theory* (Wiley-VCH Verlag GmbH, Weinheim (Federal Republic of Germany), 2000).

[14] E. Tapavicza, G. D. Bellchambers, J. C. Vincent, and F. Furche, Phys. Chem. Chem. Phys. **15**, 18336 (2013).

[15] J. C. Tully, J. Chem. Phys. **93**, 1061 (1990).

[16] C. A. Coulson and I. Fischer, The London, Edinburgh, and Dublin Philosophical Magazine and Journal of Science **40**, 386 (1949).

[17] J. Franck and E. G. Dymond, Trans. Faraday Soc. **21**, 536 (1926).

[18] E. Condon, Phys. Rev. **28**, 1182 (1926).

[19] M. Kasha, Discuss. Faraday Soc. **9**, 14 (1950).

[20] E. Schrödinger, Phys. Rev. **28**, 1049 (1926).

[21] M. Born and R. Oppenheimer, Ann. Phys. **389**, 457 (1927).

[22] B. T. Sutcliffe, Mol. Phys. **104**, 715 (2006).

[23] J. C. Tully, J. Chem. Phys. , 22A301 (2012).

[24] H. Eyring, J. Chem. Phys. **3**, 107 (1935).

[25] J. M. Bowman and B. C. Shepler, Annu. Rev. Phys. Chem. **62**, 531 (2011).

[26] D. G. Truhlar and B. C. Garrett, Annu. Rev. Phys. Chem. **35**, 159 (1984).

[27] C. E. Hornsby and R. S. Paton, Nat. Chem. **6**, 88 (2014).

[28] D. Townsend, S. A. Lahankar, S. K. Lee, S. D. Chambreau, A. G. Suits, X. Zhang, J. Rheinecker, L. B. Harding, and J. M. Bowman, Science **306**, 1158 (2004).

[29] Y. J. Hong and D. J. Tantillo, Nat. Chem. **6**, 104 (2014).

[30] B. R. Heazlewood, M. J. T. Jordan, S. H. Kable, T. M. Selby, D. L. Osborn, B. C. Shepler, B. J. Braams, and J. M. Bowman, Proc. Natl. Acad. Sci. USA **105**, 12719 (2008).

[31] T. Azumi and K. Matsuzaki, Photochem. Photobiol. **25**, 315 (1977).

[32] F. Weigend and R. Ahlrichs, Phys. Chem. Chem. Phys. **7**, 3297 (2005).

[33] J. P. Perdew, M. Ernzerhof, and K. Burke, J. Chem. Phys. **105**, 9982 (1996).

[34] P. Hohenberg and W. Kohn, Phys. Rev. **136**, B864 (1964).

[35] W. Kohn and L. J. Sham, Phys. Rev. **140**, A1133 (1965).

[36] N. T. Maitra, F. Zhang, R. J. Cave, and K. Burke, J. Chem. Phys. **120**, 5932 (2004).

[37] M. E. Casida, *Time-Dependent Density Functional Response Theory of Molecular Systems: Theory, Computational Methods, and Functionals*, edited by J. M. Seminario, Theoretical and Computational Chemistry, Vol. 4 (Elsevier, 1996).

[38] R. Bauernschmitt and R. Ahlrichs, Chem. Phys. Lett. **256**, 454 (1996).

[39] R. E. Stratmann, G. E. Scuseria, and M. J. Frisch, J. Chem. Phys. **109**, 8218 (1998).

[40] F. Furche, J. Chem. Phys. **114**, 5982 (2001).

[41] S. Hirata and M. Head-Gordon, Chem. Phys. Lett. **314**, 291 (1999).

[42] H. Hellmann, *Einführung in die Quantenchemie* (Deuticke Verlag, Leipzig, 1937).

[43] R. P. Feynman, Phys. Rev. **56**, 340 (1939).

[44] M. F. Herman, J. Chem. Phys. **76**, 2949 (1982).

[45] M. F. Herman, J. Chem. Phys. **79**, 2771 (1983).

[46] M. F. Herman, J. Chem. Phys. **81**, 754 (1984).

[47] M. F. Herman, J. Chem. Phys. **87**, 4779 (1987).

[48] T. J. Martinez, M. Ben-Nun, and R. D. Levine, J. Phys. Chem. **100**, 7884 (1996).

[49] L. Sporkel and W. Thiel, J. Chem. Phys. **144**, 194108 (2016).

[50] E. Tapavicza, I. Tavernelli, and U. Rothlisberger, Phys. Rev. Lett. **98** (2007), 10.1103/PhysRevLett.98.023001.

[51] K. J. H. Giesbertz and E. J. Baerends, Chem. Phys. Lett. **461**, 338 (2008).

[52] M. E. Casida, J. Chem. Phys. **122**, 054111 (2005).

[53] Z. Li, W. Liu, Y. Zhang, and B. Suo, J. Chem. Phys. **134**, 134101 (2011).

[54] Perdew, Burke, and Ernzerhof, Phys. Rev. Lett. **77**, 3865 (1996).

[55] M. J. G. Peach, M. J. Williamson, and D. J. Tozer, J. Chem. Theory Comput. **7**, 3578 (2011).

[56] R. Bauernschmitt and R. Ahlrichs, J. Chem. Phys. **104**, 9047 (1996).

[57] M. E. Casida, F. Gutierrez, J. Guan, F.-X. Gadea, D. Salahub, and J.-P. Daudey, J. Chem. Phys. **113**, 7062 (2000).

[58] M. Häser and R. Ahlrichs, J. Comput. Chem. **10**, 104 (1989).

[59] L. Verlet, Phys. Rev. **159**, 98 (1967).

[60] R. Gomes and M. E. Meek, J. Environ. Sci. Health, Part C **19**, 1 (2001).

[61] F. J. C. Roe and D. Wood, Indoor Built Environ. **1**, 8 (1992).

[62] K. C. Thompson, D. L. Crittenden, S. H. Kable, and M. J. T. Jordan, J. Chem. Phys. **124**, 044302 (2006).

[63] P. A. Leighton and F. E. Blacet, J. Am. Chem. Soc. **55**, 1766 (1933).

[64] Y. Kurosaki, Chem. Phys. Lett. **421**, 549 (2006).

[65] Y. Kurosaki and K. Yokoyama, Chem. Phys. Lett. **371**, 568 (2003).

[66] G. de Wit, B. R. Heazlewood, M. S. Quinn, A. T. Maccarone, K. Nauta, S. A. Reid, M. J. T. Jordan, and S. H. Kable, Faraday Discuss. **157**, 227 (2012).

[67] M. N. D. S. Cordeiro, E. Martinez, A. Fernández-Ramos, and S. A. Vázquez, Chem. Phys. Lett. **381**, 37 (2003).

[68] B. F. Gherman, R. A. Friesner, T.-H. Wong, Z. Min, and R. Bersohn, J. Chem. Phys. **114**, 6128 (2001).

[69] R. A. King, W. D. Allen, and H. F. Schaefer, J. Chem. Phys. **112**, 5585 (2000).

[70] H. Tachikawa and N. Ohta, Chem. Phys. Lett. **224**, 465 (1994).

[71] O. Setokuchi, S. Matuzawa, and Y. Shimizu, Chem. Phys. Lett. **284**, 19 (1998).

[72] J. S. Yadav and J. D. Goddard, J. Chem. Phys. **84**, 2682 (1986).

[73] H. A. Cruse and T. P. Softley, J. Chem. Phys. **122**, 124303 (2005).

[74] P. Morajkar, A. Bossolasco, C. Schoemaecker, and C. Fittschen, J. Chem. Phys. **140**, 214308 (2014).

[75] C.-L. Huang, V. Chien, C.-K. Ni, A. H. Kung, and I.-C. Chen, J. Phys. Chem. A **104**, 10362 (2000).

[76] G.-H. Leu, C.-L. Huang, S.-H. Lee, Y.-C. Lee, and I.-C. Chen, J. Chem. Phys. **109**, 9340 (1998).

[77] S.-H. Lee and I.-C. Chen, Chem. Phys. **220**, 175 (1997).

[78] T. Gejo, H. Bitto, and J. R. Huber, Chem. Phys. Lett. **261**, 443 (1996).

[79] S.-H. Lee and I.-C. Chen, J. Chem. Phys. **105**, 4597 (1996).

[80] A. C. Terentis, M. Stone, and S. H. Kable, J. Phys. Chem. **98**, 10802 (1994).

[81] J. M. Price, J. A. Mack, G. v. Helden, X. Yang, and A. M. Wodtke, J. Phys. Chem. **98**, 1791 (1994).

[82] T. Gejo, M. Takayanagi, T. Kono, and I. Hanazaki, Chem. Phys. Lett. **218**, 343 (1994).

[83] T. Kono, M. Takayanagi, and I. Hanazaki, J. Phys. Chem. **97**, 12793 (1993).

[84] T. Kono, M. Takayanagi, T. Nishiya, and I. Hanazaki, Chem. Phys. Lett. **201**, 166 (1993).

[85] A. Horowitz and J. G. Calvert, J. Phys. Chem. **86**, 3105 (1982).

[86] A. Horowitz, C. J. Kershner, and J. G. Calvert, J. Phys. Chem. **86**, 3094 (1982).

[87] H. Liu, E. C. Lim, C. Munoz-Caro, A. Nino, R. H. Judge, and D. C. Moule, J. Chem. Phys. **105**, 2547 (1996).

[88] P. L. Houston and S. H. Kable, Proc. Natl. Acad. Sci. USA **103**, 16079 (2006).

[89] K. L. K. Lee, M. S. Quinn, A. T. Maccarone, K. Nauta, P. L. Houston, S. A. Reid, M. J. T. Jordan, and S. H. Kable, Chem. Sci. **5**, 4633 (2014).

[90] L. Rubio-Lago, G. A. Amaral, A. Arregui, J. Gonzalez-Vazquez, and L. Banares, Phys. Chem. Chem. Phys. **14**, 6067 (2012).

[91] L. Rubio-Lago, G. A. Amaral, A. Arregui, J. G. Izquierdo, F. Wang, D. Zaouris, T. N. Kitsopoulos, and L. Banares, Phys. Chem. Chem. Phys. **9**, 6123 (2007).

[92] B. C. Shepler, B. J. Braams, and J. M. Bowman, J. Phys. Chem. A **111**, 8282 (2007).

[93] B. C. Shepler, B. J. Braams, and J. M. Bowman, J. Phys. Chem. A **112**, 9344 (2008).

[94] Y.-C. Han, B. C. Shepler, and J. M. Bowman, J. Phys. Chem. Lett. **2**, 1715 (2011).

[95] S.-H. Lee, J. Chem. Phys. **131**, 174312 (2009).

[96] B. G. Levine, C. Ko, J. Quenneville, and T. J. Martínez, Mol. Phys. **104**, 1039 (2006).

[97] F. Furche and R. Ahlrichs, J. Chem. Phys. **117**, 7433 (2002).

[98] A. SchaÌĹfer, H. Horn, and R. Ahlrichs, J. Chem. Phys. **97**, 2571 (1992).

[99] F. Weigend, F. Furche, and R. Ahlrichs, J. Chem. Phys. **119**, 12753 (2003).

[100] R. Send and F. Furche, J. Chem. Phys. **132**, 044107 (2010).

[101] K. Eichkorn, O. Treutler, H. Öhm, M. Häser, and R. Ahlrichs, Chem. Phys. Lett. **242**, 652 (1995).

[102] D. Rappoport and F. Furche, J. Chem. Phys. **122**, 064105 (2005).

[103] S. D. Elliott, R. Ahlrichs, O. Hampe, and M. M. Kappes, Phys. Chem. Chem. Phys. **2**, 3415 (2000).

[104] T. Williams, C. Kelley, *et al.*, "Gnuplot 4.6: an interactive plotting program," (2013).

[105] S.-H. Lee, C.-H. Chin, and C. Chaudhuri, Chem. Phys. Chem. **12**, 753 (2011).